Shallow creep on the Haiyuan Fault (Gansu, China) revealed by SAR Interferometry

R. Jolivet,[1,2] C. Lasserre,[1] M.-P. Doin,[3] S. Guillaso,[3] G. Peltzer,[4,5] R. Dailu,[6] J. Sun,[7] Z.-K. Shen,[4] and X. Xu[7]

Received 30 July 2011; revised 6 April 2012; accepted 20 April 2012; published 5 June 2012.

[1] Interferometric synthetic aperture radar data are used to map the interseismic velocity field along the Haiyuan fault system (HFS), at the north-eastern boundary of the Tibetan plateau. Two M $\sim$ 8 earthquakes ruptured the HFS in 1920 and 1927, but its 260 km-long central section, known as the Tianzhu seismic gap, remains unbroken since $\sim$1000 years. The Envisat SAR data, spanning the 2003–2009 period, cover about 200 $\times$ 300 km^2 along three descending and two ascending tracks. Interferograms are processed using an adapted version of ROI_PAC. The signal due to stratified atmospheric phase delay is empirically corrected together with orbital residuals. Mean line-of-sight velocity maps are computed using a constrained time series analysis after selection of interferograms with low atmospheric noise. These maps show a dominant left-lateral motion across the HFS, and reveal a narrow, 35 km-long zone of high velocity gradient across the fault in between the Tianzhu gap and the 1920 rupture. We model the observed velocity field using a discretized fault creeping at shallow depth and a least squares inversion. The inferred shallow slip rate distribution reveals aseismic slip in between two fully locked segments. The average creep rate is $\sim$5 mm yr^{-1}, comparable in magnitude with the estimated loading rate at depth, suggesting no strain accumulation on this segment. The modeled creep rate locally exceeds the long term rate, reaching 8 mm yr^{-1}, suggesting transient creep episodes. The present study emphasizes the need for continuous monitoring of the surface velocity in the vicinity of major seismic gaps in terms of seismic hazard assessment.

Citation: Jolivet, R., C. Lasserre, M.-P. Doin, S. Guillaso, G. Peltzer, R. Dailu, J. Sun, Z.-K. Shen, and X. Xu (2012), Shallow creep on the Haiyuan Fault (Gansu, China) revealed by SAR Interferometry, *J. Geophys. Res.*, *117*, B06401, doi:10.1029/2011JB008732.

1. Introduction

[2] The recent improvements in space-based geodesy, with the increasing number and accuracy of surface deformation measurements, allow us to better investigate the stress and strain distribution and evolution within the lithosphere throughout the seismic cycle. Coseismic and postseismic deformations are now well described and modeled, based on InSAR and GPS data, in particular. In contrast, measuring and modeling spatiotemporal variations of the interseismic deformation along a fault remain difficult and are now at the forefront of the research in seismotectonics and seismic hazard assessment.

[3] Recent advances on this topic have come from the study of subduction zones, with the discovery of slow slip events (e.g., Japan [*Ozawa et al.*, 2002], Cascadia [*Dragert et al.*, 2001], Mexico [*Kostoglodov et al.*, 2003; *Radiguet et al.*, 2011]) and lateral variations of interseismic coupling [e.g., *Mazzotti et al.*, 2000; *Chlieh et al.*, 2008]. Transient or permanent aseismic slip during the interseismic period have also been observed along sections of intracontinental strike-slip faults (e.g., North Anatolian Fault [*Ambraseys*, 1970; *Çakir et al.*, 2005], San Andreas fault [*Lienkaemper et al.*, 1991; *Schmidt et al.*, 2005; *Ryder and Bürgmann*, 2008]) or normal faults [e.g., *Doubre and Peltzer*, 2007]. Aseismic slip may reduce seismic hazard by releasing stress in the seismogenic

[1]Institut des Sciences de la Terre, UMR 5275, Université Joseph Fourier, CNRS, Grenoble, France.
[2]Now at Tectonic Observatory, California Institute of Technology, Pasadena, California, USA.
[3]Laboratoire de Géologie, UMR 8538, Ecole Normale Supérieure, CNRS, Paris, France.
[4]Department of Earth and Space Science, University of California, Los Angeles, California, USA.
[5]Jet Propulsion Laboratory, California Institute of Technology, Pasadena, California, USA.
[6]Lanzhou Seismological Institute, Chinese Earthquake Administration, Lanzhou, China.
[7]Institute of Geology, Chinese Earthquake Administration, Beijing, China.

Corresponding author: R. Jolivet, Tectonic Observatory, California Institute of Technology, Pasadena, CA 90125, USA. (romain.jolivet@ujf-grenoble.fr)

0148-0227/12/2011JB008732

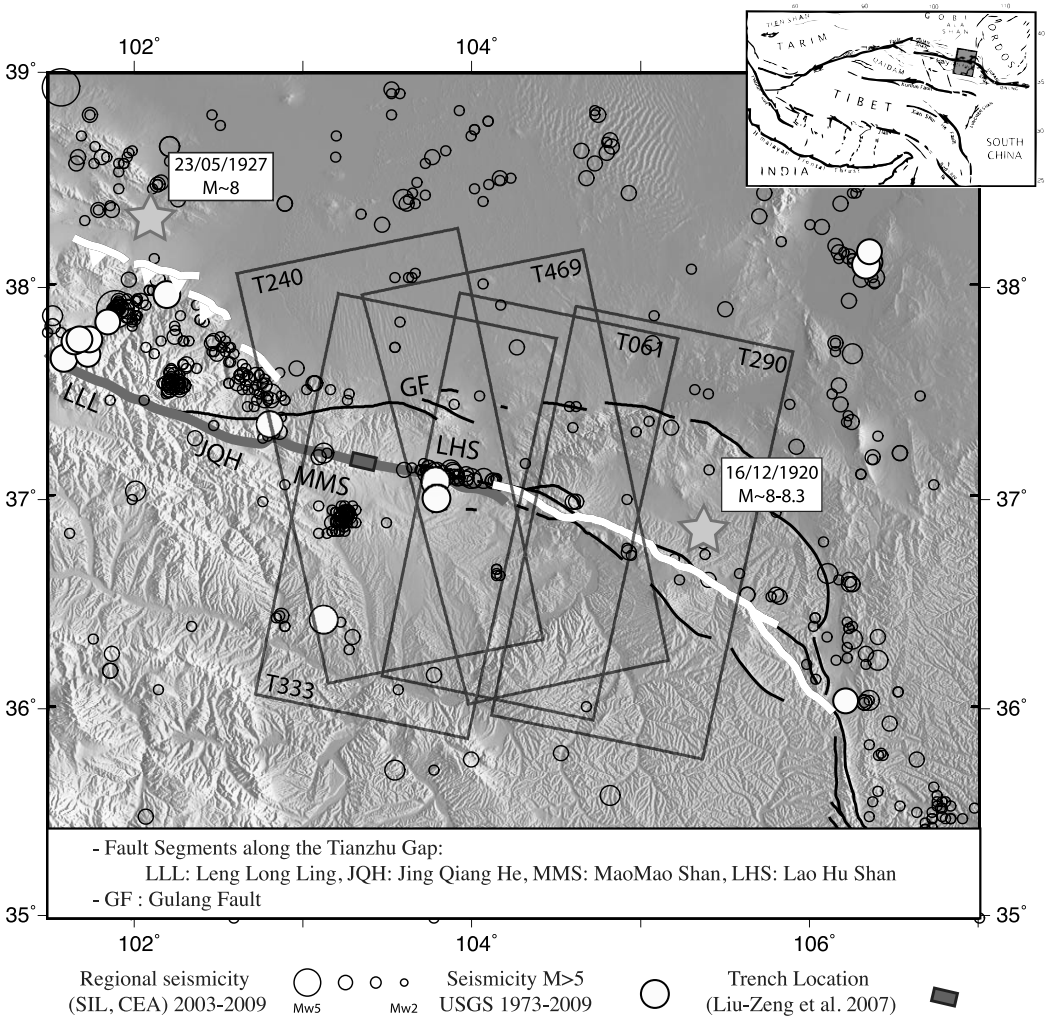

Figure 1. Seismotectonic map showing the Haiyuan Fault system and its location in the India-Asia collision zone. Fault traces are superimposed on Shuttle Radar Topography Mission (SRTM) Digital Elevation Model (DEM). White lines and stars represent surface ruptures and epicenters, respectively, of the M ∼ 8 1920 and 1927 earthquakes. Bold grey line follows the Tianzhu seismic gap [*Gaudemer et al.*, 1995]. Black rectangles shows the coverage of analyzed Envisat SAR data, with track numbers indicated. Seismicity from Seismological Institute of Lanzhou, Chinese Earthquake Administration regional network is shown for the 2003–2009 period.

part of the crust. It may also play an important role in the triggering of large ruptures, as shown by numerical simulation [*Lapusta and Liu*, 2009] and recent seismic observations [*Bouchon et al.*, 2011]. Recent studies thus point to the importance of studying the spatial patterns and rates of strain accumulation during the interseismic phase, the mechanisms involved and their relationship with the physical properties of faults and their surrounding graphic [*Hetland and Hager*, 2006; *Lundgren et al.*, 2009; *Jolivet et al.*, 2009]. Such observations remain challenging and only a few faults are currently well documented.

[4] We focus here on the Haiyuan fault system at the northeastern margin of the Tibetan plateau. Two M_w 8 earthquakes ruptured long sections of this fault system in the past century (1920, 1927, Figure 1). Another section has been identified as a seismic gap with a high hazard [*Gaudemer et al.*, 1995], and possible shallow creep at its eastern end, as suggested by a previous InSAR study based on sparse ERS data [*Cavalié et al.*, 2008]. This makes the Haiyuan fault an interesting target to investigate along-strike variations of the interseismic strain rate in relation with the fault seismic history and geometry.

[5] We use Envisat SAR interferometry data to map the mean surface displacement rate in the fault area between 2003 and 2009. Given the low expected strain rate, methodological refinements are required [*Cavalié et al.*, 2008]. We first present the seismotectonic setting of the Haiyuan fault system, the radar data set, and the overall processing strategy. We then detail specific InSAR processing steps developed to increase the signal-to-noise ratio, including atmospheric phase delay correction, interferogram selection, and time series analysis. We model the 2-D interseismic strain rate

Table 1. Envisat Data Set, Interferogram Selection for Time Series Analysis and Residual Turbulent Noise Model on LOS Velocity Maps[a]

Track	Number of Images and Interferograms	Images Used in Time Series	Interferograms Used in Time Series	Covariance Function ($rad^2\ yr^{-2}$)	Autocovariance ($rad^2\ yr^{-2}$)
T061	31 (167)	75% (23)	54% (90)	$0.0073e^{-0.1378x}$	0.0087
T240	25 (130)	60% (15)	31% (40)	$0.01473e^{-0.1487x}\cos(-0.01124x)$	0.01527
T290	25 (83)	64% (16)	35% (29)	$0.01934e^{-0.086x}\cos(-0.05649x)$	0.02225
T333	32 (163)	56% (18)	30% (47)	$0.01631e^{-0.1734x}$	0.01902
T469	21 (88)	66% (14)	45% (40)	$0.02408e^{-0.08934x}$	0.02628

[a]x is the distance that separates two pixels.

based on mean LOS velocity maps, taking into account spatially correlated residual noise. We finally discuss the implications of the observed spatial strain variations.

2. The Haiyuan Fault System

[6] The 1000 km-long Haiyuan fault system extends from the central Qilian Shan to the west, to the Liupan Shan, to the east (Figure 1). It contributes to the accomodation of the deformation related to the India/Asia collision. Strain is partitioned between predominantly left-lateral east-striking faulting, along the Haiyuan and Gulang faults, and North-North-East shortening across thrusts systems [*Gaudemer et al.*, 1995]. Left-lateral and thrusts faults connect at depth to an oblique shear zone, through a south-dipping decollement [*Gaudemer et al.*, 1995; *Meyer et al.*, 1998].

[7] Two M_w 8 earthquakes occurred on the Haiyuan fault system in the past century (Figure 1). The 12-16-1920, M_w 8–8.3, Haiyuan earthquake broke the eastern ~240 km-long section of the Haiyuan fault [e.g., *Deng et al.*, 1986; *Zhang et al.*, 1987]. The 05-23-1927, M_w 8, Gulang earthquake ruptured south-dipping thrusts located at the south-eastern end of the Qilian Shan [*Gaudemer et al.*, 1995; *Xu et al.*, 2010]. In contrast, the 260 km-long unruptured section of the Haiyuan fault, west of the 1920 rupture, has been identified as a seismic gap, the Tianzhu gap, with a high seismic hazard (Figure 1) [*Gaudemer et al.*, 1995]. From a paleoseismological study, *Liu-Zeng et al.* [2007] estimated the recurrence time of earthquakes along the Tianzhu gap to be about 1000 years, with the last two large earthquakes occurring at 1092 AD and at 143 or 374 AD (estimated M_w 8). A few M_w 5–6 events have occurred near the extremities of the gap, in the past 20 years [*Lasserre et al.*, 2001]. Intense microseismic activity is also concentrated in between the 1920 rupture and the seismic gap (Figure 1).

[8] The Holocene slip rate of the Haiyuan fault was estimated from offset measurements and dating of morphological markers (alluvial terrasses and moraines). It decreases from west to east, from 19 ± 5 mm yr^{-1} along the Leng Long Ling segment [*Lasserre et al.*, 2002], to 12 ± 4 mm yr^{-1} along the Mao Mao Shan segment [*Lasserre et al.*, 1999], down to 3.5–10 mm yr^{-1} along the 1920 rupture (8 ± 2 mm yr^{-1} [*Zhang et al.*, 1988], 4.5 ± 1 mm yr^{-1} [*Li et al.*, 2009]). As for most strike-slip faults in Tibet, the short term (i.e. geodetic) slip rate of the Haiyuan fault, that may vary during its seismic cycle, differs from the average long term (i.e. Quaternary) slip rate. The cause for such discrepancy remains controversial [e.g., *Mériaux et al.*, 2004; *Cowgill*, 2007; *Loveless and Meade*, 2011]. Large scale, rigid block models based on GPS data over China [e.g., *Gan et al.*, 2007] indicate a 8.6 mm yr^{-1} slip rate on the Haiyuan fault. *Cavalié et al.* [2008] derive a 4.2–8 mm yr^{-1} slip rate from the modeling of a fault-parallel velocity profile across the fault, near the junction between the 1920 rupture and the Tianzhu gap, using sparse ERS InSAR data between 1993 and 1998. Additionally, they highlight a strong strain concentration in the fault zone and suggest the presence of creep at shallow depth. In the following sections, we further characterize the interseismic slip rate on the fault, and its along-strike variations at shallow depth based on denser time series of InSAR data, covering an extended study area and period.

3. Envisat Data Set and Interferogram Processing

[9] We process all available radar data acquired by the ENVISAT satellite from two ascending and three descending orbital tracks, to measure the interseismic deformation along the Haiyuan fault system (Figure 1). This data set covers the eastern part of the Tianzhu gap as well as the western end of the 1920 rupture, over a 60000 km^2 area. Data span the 2003–2009 period, with almost monthly acquisitions since 2007. 21 to 32 images are combined into 83 to 167 interferograms, depending on the track number (Table 1).

[10] We use an interferometric chain that includes routines from the ROI_PAC software [*Rosen et al.*, 2004] and additional modules to process raw data into interferograms [*Doin et al.*, 2011]. Precise DORIS orbits are provided by the European Space Agency. We use the Shuttle Radar Topography Mission Digital Elevation Model [*Farr and Kobrick*, 2000] oversampled by a factor of 2 after referencing to the WGS84 ellipsoid. The main processing steps are the following:

[11] 1. Single Look Complex (SLC) images are computed with a common doppler, chosen so that their doppler bandwidths overlap with each other at 90% minimum.

[12] 2. We select a single master image that maximizes the total coherence, following *Zebker and Villasenor* [1992] and *Hooper et al.* [2007].

[13] 3. All SLCs are coregistered in the master image geometry using a Digital Elevation Model (DEM) assisted procedure [*Nitti et al.*, 2011]. This procedure is described in the Appendix A.

[14] 4. We select image pairs with a perpendicular baseline smaller than 400 meters and a temporal baseline greater than six months, following a Small BAseline Subset approach (SBAS) [*Berardino et al.*, 2002]. This provides a good compromise in terms of interferograms signal-to-noise ratio and coherence.

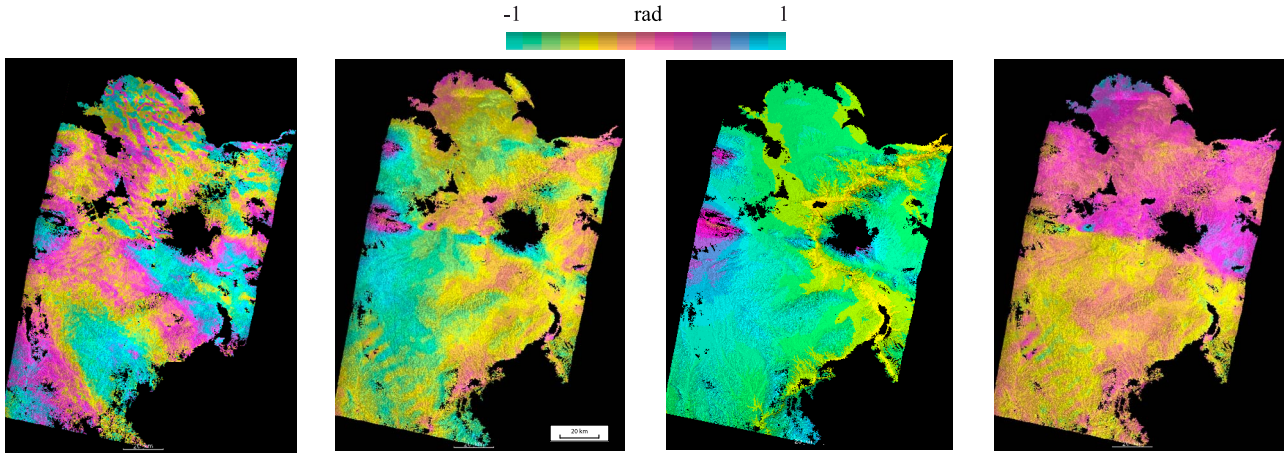

(a) 06/26/2004-01/12/2008 (b) 12/18/2004-12/01/2008 (c) DEM (SRTM) (d) corrected from the stratified delay

Figure 2. Examples of interferograms showing (a) turbulent atmospheric patterns and (b) stratified atmospheric phase delay correlated with elevation. (c) Digital Elevation Model from SRTM, one color cycle represents 350 meter elevation change. (d) Same as Figure 2b after correction from stratified atmospheric delay and orbital errors. One color cycle represents 2 rad along LOS.

[15] 5. Full resolution differential interferograms are obtained after range spectral filtering adapted to the local elevation slope [*Guillaso et al.*, 2006, 2008]. Steps 3 and 5 improve the coherence at long perpendicular baselines in areas of rough topography. Interferograms are corrected from orbital effects and topography, using precise DORIS orbits and the SRTM DEM.

[16] 6. Interferograms are looked by a factor of 4 in range and of 20 in azimuth, filtered using a power spectrum filter [*Goldstein and Werner*, 1998], and unwrapped using a branch-cut algorithm [*Goldstein et al.*, 1988].

[17] 7. Finally, we perform an atmospheric mitigation process and a time series analysis, as described in the following sections. These procedures allow us to recover the phase increments between two acquisition dates.

4. Correction of Atmospheric Phase Delay and Orbital Errors

[18] The unwrapped differential interferometric phase $\Phi_{i,j}$ between two dates i and j can be written as the sum of four terms:

$$\Phi_{i,j} = \phi_{def} + \phi_{orbit} + \phi_{atmo} + \phi_{noise}, \quad (1)$$

where ϕ_{def} is the expected deformation signal related to the fault, ϕ_{orbit} is the residual orbital phase, ϕ_{atmo} the atmospheric phase delay and ϕ_{noise} the residual noise from instrument, decorrelation, coregistration, unwrapping or DEM errors.

4.1. Tropospheric Phase Delays

[19] As phase delays related to dispersive effects in the ionosphere can be neglected in C-band radar, we consider here only the tropospheric propagation delays, related to the spatial and temporal variability of the air refractivity index. Tropospheric delays are separated into a stratified component, corresponding to the vertical stratification averaged over the scene, and a turbulent term, that is considered random in space and time (Figure 2a). The turbulent portion of the troposphere delay can be efficiently removed by interferogram stacking [e.g., *Zebker et al.*, 1997; *Ryder and Bürgmann*, 2008] or time series analysis [e.g., *Ferretti et al.*, 2001; *Schmidt and Bürgmann*, 2003]. The "stratified" component of the tropospheric phase delay (Figure 2b) only depends on the temporal variations of the troposphere vertical stratification in between the minimum and maximum elevations of a scene [*Doin et al.*, 2009, and references therein]. It is related to elevation and mimicks topography on interferograms (Figures 2b and 2c). It is highly problematic in cases where topography correlates with the expected tectonic signal (e.g., Kunlun fault [*Jolivet et al.*, 2011]). Estimates of displacement rates may be biased by stratified delays, because of the uneven sampling throughout the season cycle [*Doin et al.*, 2009].Therefore, such delays must be corrected prior to or during the time series analysis [*Elliott et al.*, 2008].

4.2. Correction Strategy

[20] To account for trade-offs between ϕ_{def}, ϕ_{orbit} and ϕ_{atmo}, we estimate these contributions through a joint inversion [*Cavalié et al.*, 2008]. We use the following simplified expression of equation (1):

$$\Phi_{i,j} = \sigma_{i,j}D + \alpha_{i,j}R + \beta_{i,j}A + \gamma_{i,j}RA + \delta_{i,j} + k_{i,j}z + \phi_{rand} + \phi_{noise}. \quad (2)$$

[21] The first term corresponds to ϕ_{def}. It is scaled to D, an interseismic elastic half-space model, projected in the satellite Line-Of-Sight (hereafter referred to as LOS) [*Savage and Burford*, 1973; *Cavalié et al.*, 2008]. The second, third, fourth and fifth terms correspond to ϕ_{orbit}, a function of the range R and the azimuth A. We use a bilinear function to describe ϕ_{orbit} because of a lack of additional independent constraints on the orbital contribution (equation (2)).The

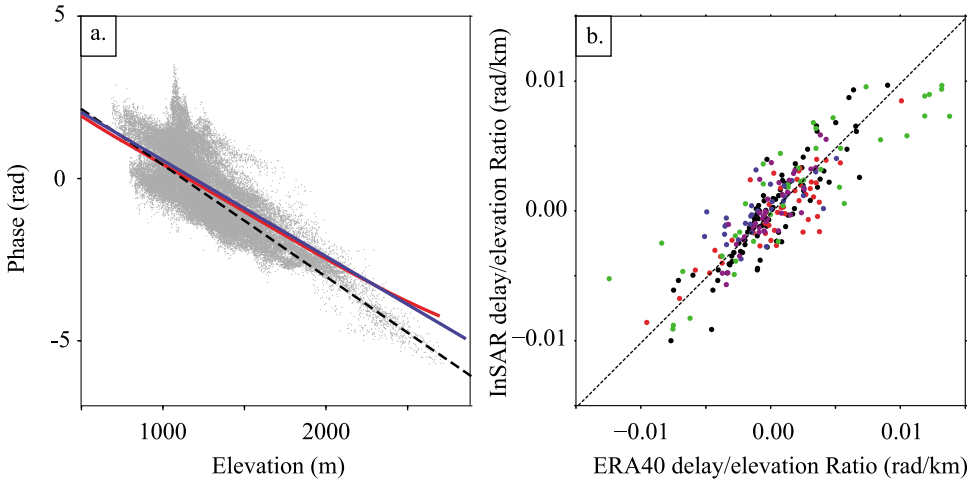

Figure 3. (a) Phase/Elevation correlation plot from Figure 2b (gray dots). Blue line is the linear fit to data. Red curve is the prediction from global atmospheric model ERA40. Black dashed line is the linear trend, inverted through a time series analysis, used to correct interferograms, as shown in Figure 2d. (b) Comparison between delay/elevation ratios derived from InSAR data and ERA40 model. Black/red/green/blue/purple dots represents respectively tracks 061/333/290/469/240. Black dashed line represents the unit correlation. The regression coefficient is 0.71. The RMS between delay/elevation ratios derived from InSAR data and ERA40 are 0.0017 rad.km^{-1}, 0.0013 rad.km^{-1}, 0.003 rad.km^{-1}, 0.0019 rad.km^{-1} and0.002 rad.km^{-1} for tracks 061, 240, 290, 333, and 469, respectively.

sixth term corresponds to ϕ_{atmo}, which is divided into a stratified tropospheric phase delay, approximated by a linear function of the elevation z, and a turbulent contribution ϕ_{rand}.

[22] For each interferogram, produced with acquisitions i and j, we jointly solve for parameters $\sigma_{i,j}$, $\alpha_{i,j}$, $\beta_{i,j}$, $\gamma_{i,j}$ and $k_{i,j}$ using a least squares minimization. To ensure that stratified delay corrections are consistent within the interferogram network, we reestimate the delay/elevation ratios $k_{i,j}$ through a time series analysis [*Cavalié et al.*, 2007; *Elliott et al.*, 2008]. Orbital parameters are reestimated in a similar way [*Biggs et al.*, 2007].

[23] All interferograms are corrected using the derived orbital and stratified delay contributions. Figures 2d and 3a show an example of such correction, which illustrates the validity of the delay/elevation linear trend approximation, as observed on most of the interferograms because of the moderate elevation range across the scene. The delay/elevation relationship reestimated with a network approach shows a better agreement with the InSAR data, from low to high elevation.

4.3. Correction Validation

[24] Global atmospheric models allow the computation of the stratified tropospheric phase delay as a function of elevation as well as the corresponding delay/elevation ratio [*Doin et al.*, 2009]. We compare the InSAR derived delay/elevation ratios with prediction from the ERA40 analysis provided by the European Centre for Medium-Range Weather Forecast (Figure 3) [*Uppala et al.*, 2005].

[25] For each acquisition date, we extract the specific humidity, the temperature and the geopotential height at each of the 21 pressure levels at one grid point per track chosen at the lowest elevation within the studied area. Parameters are taken at 6 AM and 6 PM, for descending and ascending tracks respectively. We then generate ERA-derived delay/elevation ratios for all interferograms.

[26] Figure 3b shows the good agreement between InSAR derived and ERA40 derived delay/elevation ratios, with only minor differences from one track to another. Discrepancies for some interferograms may be due to the prevailance of turbulences, to a complex vertical stratification of the troposphere with a non-linear delay/elevation relationship, or to poorly constrained model parameters at some dates.

5. Time Series Analysis

[27] After interferogram corrections from residual orbital errors, phase/elevation correlation and referencing, we produce mean LOS velocity maps for each track, to investigate for spatial variations of interseismic strain across the Haiyuan fault. Interferogram stacking is one way to compute mean LOS velocity maps [e.g., *Peltzer et al.*, 2001; *Wright et al.*, 2001]. It reduces random noise by a factor of $\sqrt{N}$, if N independent interferograms are used [*Zebker et al.*, 1997]. However, it requires proper selection and weighting of interferograms, based on their signal-to-noise ratios [*Cavalié et al.*, 2008] and corrections of tropospheric phase delays beforehand to obtain reliable, unbiased velocity estimates [*Cavalié et al.*, 2008; *Doin et al.*, 2009]. Time series analysis is preferably used for large sets of interferograms [e.g., *Usai*, 1999; *Ferretti et al.*, 2001; *Berardino et al.*, 2002; *Schmidt and Bürgmann*, 2003; *Hooper et al.*, 2007; *Cavalié et al.*, 2007]. It preserves data ordering through time and takes advantages of redundancy in the spatial and temporal baseline spaces, so that time-dependent ground deformation can be distinguished from random atmospheric noise, unwrapping and DEM errors.

[28] We follow a variant of the SBAS approach [*Berardino et al.*, 2002] described by *Lopez-Quiroz et al.* [2009] to build

the displacement time series and derive best fit interseismic velocity maps.

5.1. Constrained Time Series

[29] For each pixel of each track, independently, we consider the following linear equation system:

$$\Phi_{i,j} = \sum_{k=i}^{j-1} \delta\varphi^k \quad \text{and} \quad \varphi^1 = 0, \tag{3}$$

where φ^1 is the phase value at the first acquisition date among N in the data set, and $\Phi_{i,j}$ is the pixel interferometric phase between dates i and j, and $\delta\varphi^k$ are phase increments between successive dates k and $k + 1$. For some pixels, the interferogram network may be separated into independent groups of interferograms, with no geometrical and temporal overlap. Equation (3) is usually inverted using a Singular Value Decomposition method to overcome this limitation [*Berardino et al.*, 2002]. We favor the inversion approach of *Lopez-Quiroz et al.* [2009]: a linear phase model is used to connect independent groups of images, as an additional constraint to equation (3). We also take into account the phase errors that are a result of DEM errors, correlated with the perpendicular baseline. The constraining equation is then:

$$\forall l \in [2; N] \quad \sum_{k=1}^{l-1} \delta\varphi^k = \mathrm{V}\Delta t^l + e\mathrm{B}_\perp^l + c, \tag{4}$$

where V is the mean LOS velocity for the considered pixel, $\Delta t^l = t^l - t^1$ is the time interval between acquisition 1 and l, e is proportional to the DEM error, $\mathrm{B}_\perp^l$ is the perpendicular baseline of acquisition l, with respect to the first acquisition and c is a constant. We combine equations (3) and (4) and invert the corresponding linear system using a least squares minimization scheme [*Anderson et al.*, 1999] (Appendix B).

[30] We perform this inversion for each pixel that is unwrapped in at least 50% of the interferograms. In the end, we obtain for each track independently the phase increments at all pixels, the mean LOS velocity and a DEM correction map in the radar geometry.

5.2. Data Selection

[31] To improve the signal-to-noise ratio of the mean LOS velocity maps, we select images with the lowest residual atmospheric noise prior to time series analysis (Table 1). We first compute the 1-D energy function, Sp, of the residual noise, for each interferogram with at least 30% of unwrapped pixels [*Puysségur et al.*, 2007; *Cavalié et al.*, 2008]:

$$\mathrm{Sp}(x) = \frac{1}{N(x)} \sum_{m,n/dist(m,n)=x} |\Phi_m - \Phi_n|, \tag{5}$$

where $N(x)$ is the number of pairs of pixels m and n separated by a distance x, Φ_m and Φ_n are the interferometric phases of pixels m and n, respectively. The energy function (or noise spectrum) provides an estimate of the noise correlation distance ($\sim$30 km) and of the amplitude of the residual turbulent atmospheric noise for each interferogram (sill value over $\sim$30 km, Figure 4). Sp(x) increases from short distances to $\sim$30 km, over which it flattens for most interferograms.

[32] We solve for the noise spectrum at each acquisition date using a least squares inversion of interferogram spectra (Appendix C). Figures 4c and 4d show the inverted sill values of the spectra and their associated resolution, for each acquisition date on track 061. The highest (respectively lowest) spectra values mostly correspond to the summer (respectively winter) acquisitions, as previously found by from *Doin et al.* [2009].

[33] We select radar scenes with low and well resolved spectra sill values. Our tests show that the selection of scenes with a sill value below 1 rad and a resolution above 0.75 is a good compromise in terms of data set decimation and noise reduction on the LOS velocity maps. Only interferograms computed from these scenes are used in the time series analysis. About 25 to 45% of the images are eliminated, depending on the track number (Table 1). The resulting interferogram network for track 061 is shown on Figure 4a. The auxiliary material illustrates the selection process for tracks 240, 290, 333 and 469 together with the temporal coherence map [*Gourmelen et al.*, 2010].[1]

5.3. Analysis of Mean LOS Velocity Maps

[34] Figure 5 shows the LOS velocity maps obtained for two ascending and three descending tracks after georeferencing to the ground geometry. The residual noise level of the velocity maps is greatly reduced compared to that of the corresponding interferograms (Figure 4b and auxiliary material). It varies from 0.15 rad.yr^{-1} for track 061 to about 0.25 rad.yr^{-1} for track 469. This corresponds to 30–50% of the expected velocity step across the fault (0.5 rad.yr^{-1} corresponds to 6 mm yr^{-1} in fault parallel velocity, assuming a pure strike-slip motion on a vertical fault) [*Cavalié et al.*, 2008]. The higher noise level on track 469 (Figure 5) likely results from the lower quality of that data set, which has fewer images than on other tracks and is affected by a more significant turbulent tropospheric signal (Table 1).

[35] The first remarkable feature on Figure 5 is the steep LOS velocity gradient across the Haiyuan fault, on all tracks. This step has opposite signs on descending and ascending tracks, consistent with left-lateral motion, and reaches up to 0.5 rad.yr^{-1} along LOS (Figures 5 and 6). The shape of the velocity profiles across the fault is in overall consistent with a classic arctangent shape predicted by elastic models across a strike-slip fault [*Savage and Burford*, 1973]. However, along-strike variations of the strain distribution are observed, in the near fault zone in particular, due to the combination of horizontal and vertical motion or to various degrees of fault locking in the seismogenic zone.

[36] The velocity gradient across the fault varies from west to east. While rather smooth along the trace of the 1920 rupture (0.04 rad.yr^{-1}.km^{-1} on track 061, or 0.2 LOS-mm yr^{-1}.km^{-1}; Figures 5 and 6a), it becomes sharper and concentrated in a 35 km-long narrow zone along the Lao Hu Shan (LHS) segment at the eastern end of the Tianzhu gap (0.12 rad.yr^{-1}.km^{-1} on track 061 or 0.5 LOS-mm yr^{-1}.km^{-1}; Figures 5 and 6b). Furthermore, the LOS velocity step observed in the near fault zone (up to 1.4 rad.yr^{-1}, or 6 LOS-mm yr^{-1}) is higher than that in the far field (0.5 rad.yr^{-1} or 2 LOS-mm yr^{-1}; Figure 6b). These observations suggest that the upper

[1] Auxiliary materials are available in the HTML. doi:10.1029/2011JB008732.

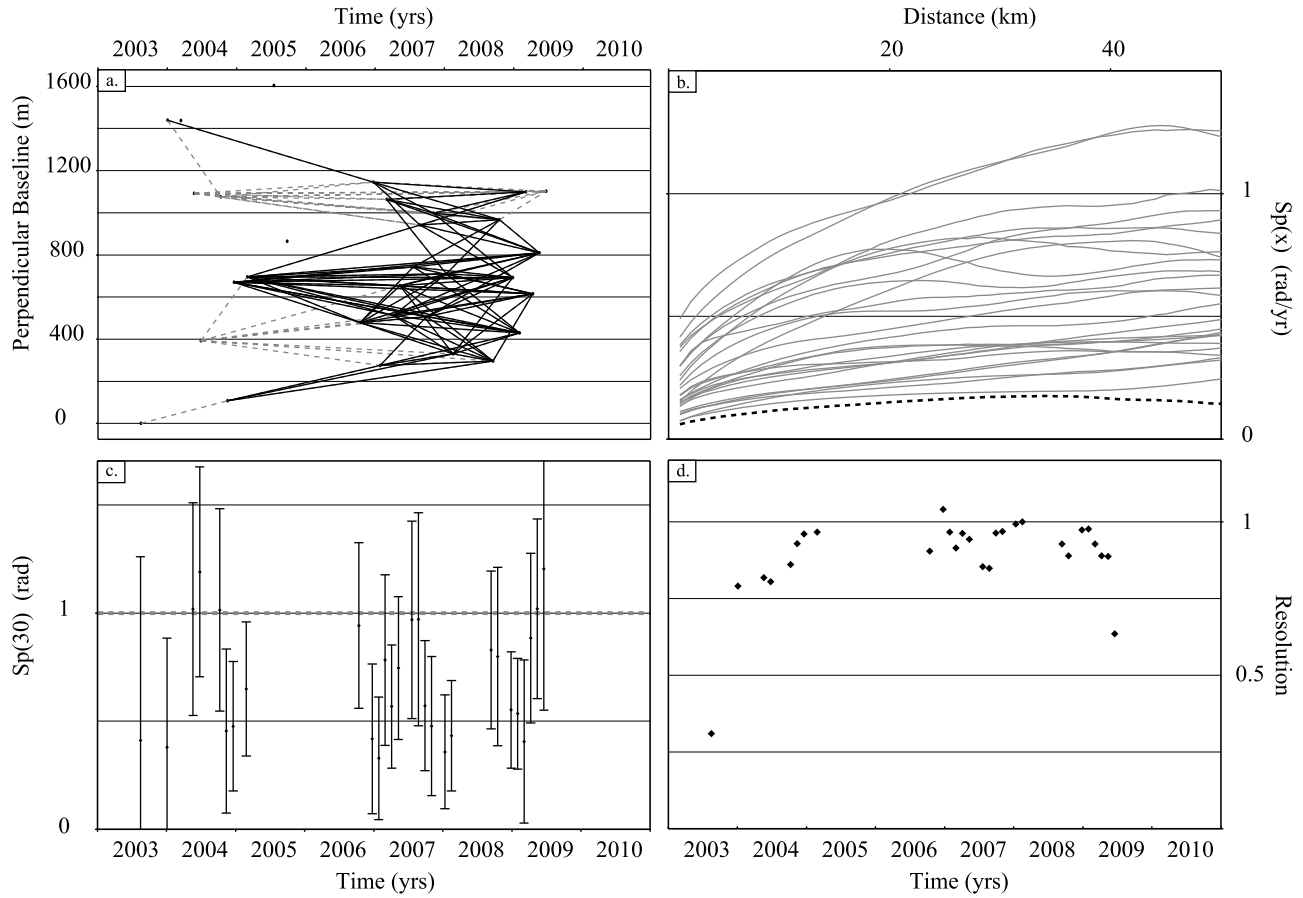

Figure 4. For Track 061: (a) Relative perpendicular baseline of all radar images as a function of their acquisition dates. Dashed lines indicate processed images pairs. Black lines show interferograms selected for Time series analysis. (b) Noise energy function Sp as a function of distance for each interferogram, normalized by the temporal baseline. Black dashed line is the mean LOS velocity map noise energy function. (c) Noise energy spectrum at 30 km for each interferogram, obtained by inversion. Error bars are 1 sigma. Acquisition with Sp(30) greater than 1 rad are rejected. (d) Resolution of inverted Sp(30) values. Acquisitions with resolution less than 0.75 are rejected.

seismogenic part of the crust is fully locked along the 1920 rupture segment and is creeping along the LHS segment, at a rate that may exceed the tectonic loading rate at depth.

[37] In between these 2 segments, the left-stepping releasing jog (~10 km-long and 5 km-wide) shows a LOS velocity increase on both ascending and descending tracks (Figures 5 and 6c). This indicates a vertical motion, away from satellite, consistent with subsidence in a pull-apart basin ("Jingtai Basin" hereafter). Other subsiding areas are visible in the central part of the 1920 rupture, most likely corresponding to mining or other human-related activities.

[38] A velocity gradient of up to 0.25 rad.yr^{-1} along the LOS is also visible about 40 km north of the Haiyuan fault and may be associated with predominantly left-lateral motion on the Gulang fault.

6. Fault Slip-Rate Modeling

[39] To investigate further the spatial variations of the strain rate along the different segments of the fault, we invert the LOS velocity maps to estimate a slip-rate on the deep part of the fault and the slip-rate distribution along its shallow part.

6.1. Model Geometry and Parametrization

[40] Our fault model is based on the following simplifications: (1) slip on the deep section of the fault, below the 20 km seismogenic depth, estimated from the micro-seismicity distribution (Figure 7) and seismological studies [*Lasserre et al.*, 2001], is assumed to be purely horizontal and uniform, (2) slip on the shallow section can vary along strike in amplitude and rake. Following, *Cavalié et al.* [2008], we assume that the fault is vertical. Its shallow part is divided into two segments, corresponding to the eastern end of the Tianzhu gap and to the 1920 rupture, following the fault surface trace mapped from satellite images and fieldwork. It is discretized into 512 2.5 × 2.5 km patches (Figure 7). The deep section of the fault is considered as a single dislocation following a smoothed trace with respect to that at the surface.

[41] We solve for (1) both the strike-slip and dip-slip components of the slip rate on the shallow patches, (2) a uniform strike-slip rate at depth, (3) a bilinear ramp in longitude and

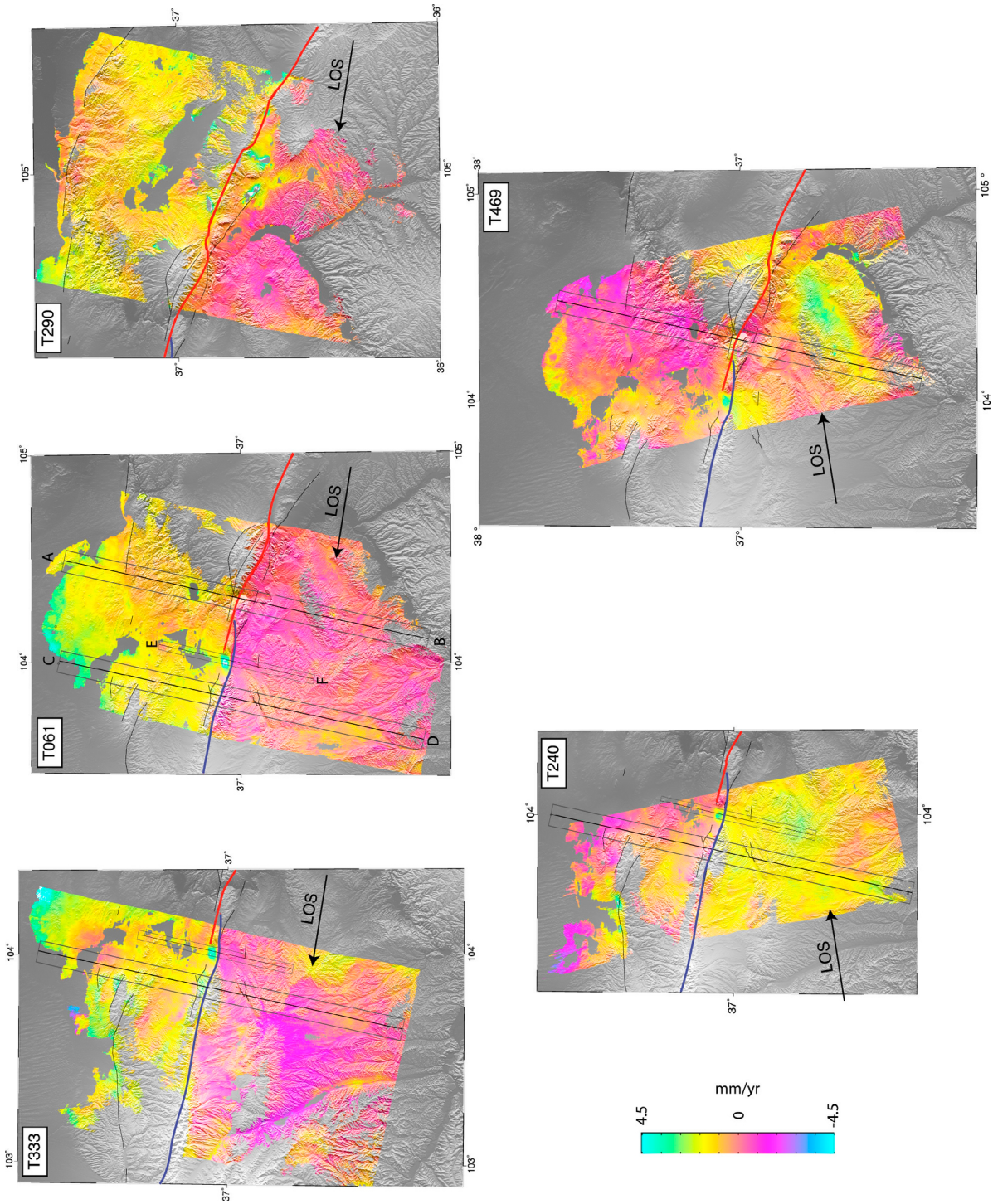

Figure 5. Mean Line-Of-Sight velocity maps from time series analysis for each track. One color cycle (yellow/pink/green) is 9 mm/yr toward the satellite. Red line follows the 1920 rupture trace along the Haiyuan fault. Blue line follows the Tianzhu seismic gap. Dark thin lines indicate secondary faults. Boxes show location of profiles on Figure 6. Background shade is from SRTM DEM.

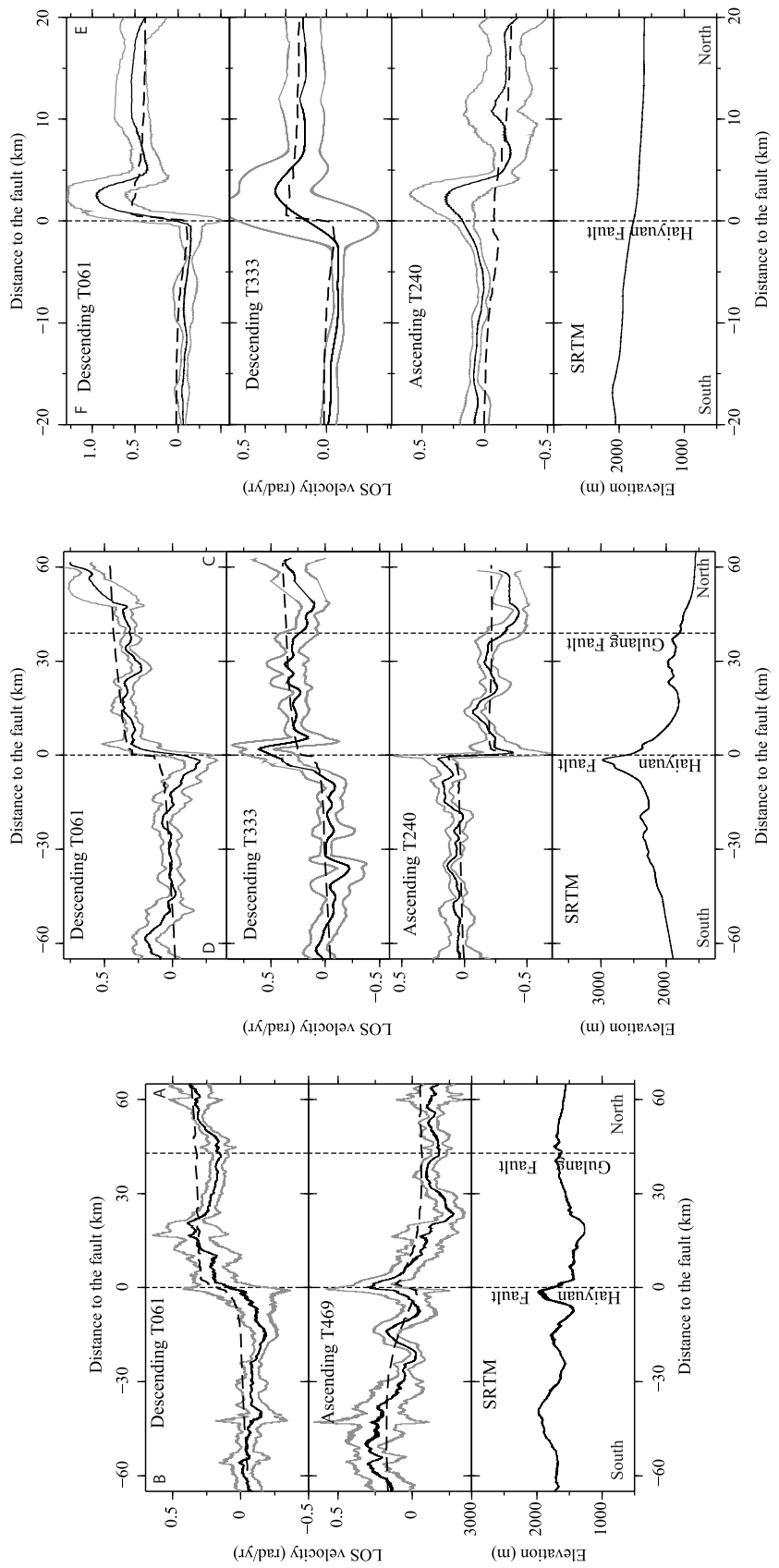

a. 1920 Rupture b. Lao Hu Shan c. Jingtai Basin

Figure 6. Mean Line-Of-Sight velocity profiles (black lines) with 2-sigma deviation (grey lines). Dashed black lines show preferred model of Figure 7, corresponding elevation profiles are shown at bottom. Profile location are shown on Figure 5: (a) 1920 rupture, (b) Tianzhu gap and (c) Jingtai Basin.

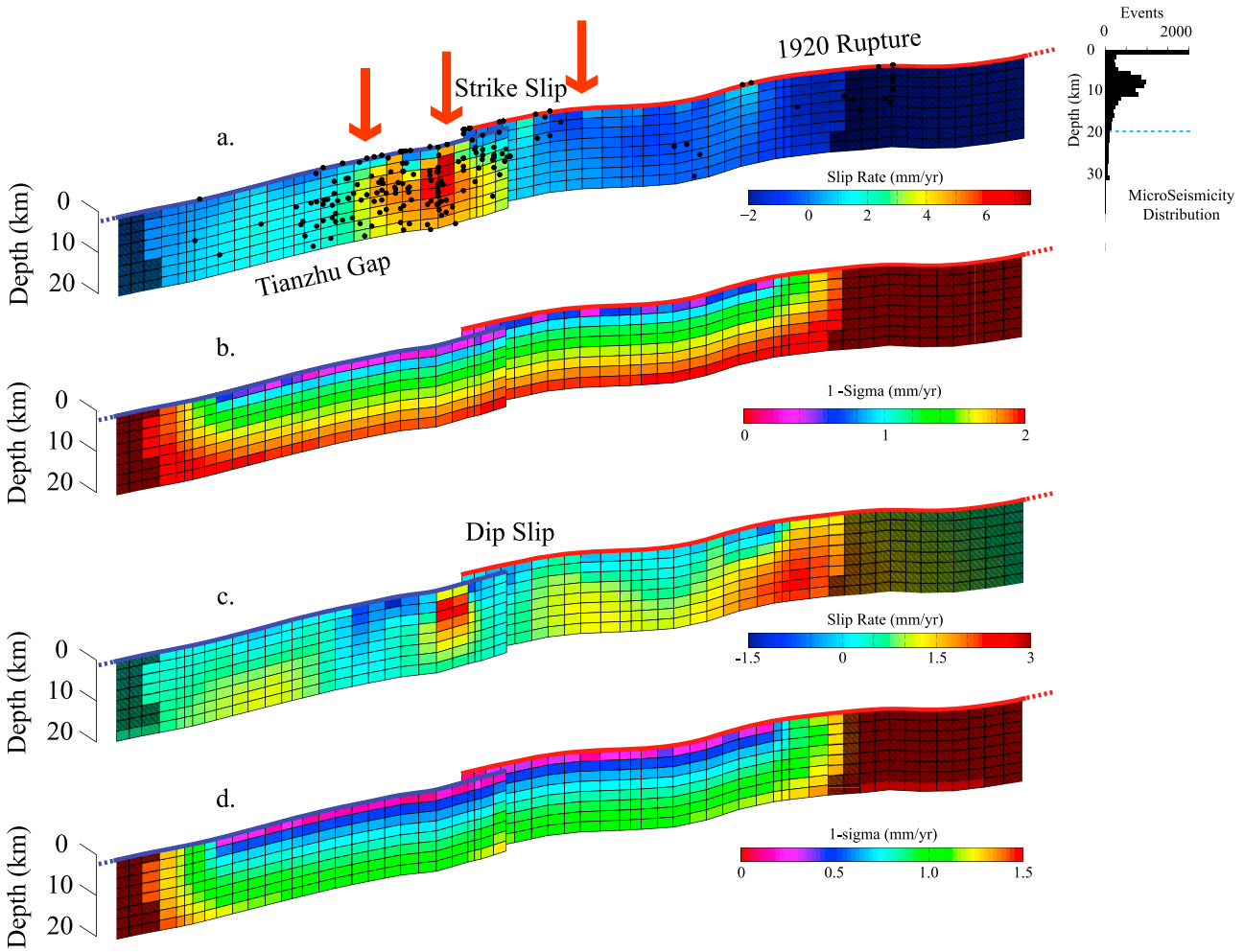

Figure 7. Vertical 2.5 × 2.5 km^2 gridded fault model in the upper 20 km, with inverted shallow slip rate distribution and associated standard deviation: (a, b) strike-slip and (c, d) dip-slip components. Positive values are for east ward and uplift motion south of the fault, respectively. Blue and red line outline the Tianzhu gap and 1920 rupture fault traces. Grey shaded fault patches correspond to patches on which model is poorly resolved (R < 0.63).

latitude and a constant to correct for residual orbital errors for each LOS velocity map. We use the generalized least squares solution [*Tarantola*, 2005]:

$$\mathbf{m}_{\text{post}} = \mathbf{m}_{\text{prior}} + (\mathbf{G}^{\mathbf{t}}\mathbf{C}_{\text{D}}^{-1}\mathbf{G} + \mathbf{C}_{\text{M}}^{-1})\mathbf{G}^{\mathbf{t}}\mathbf{C}_{\text{D}}^{-1}(\mathbf{d}_{\text{obs}} - \mathbf{G}\mathbf{m}_{\text{prior}}). \quad (6)$$

$\mathbf{m}_{\text{prior}}$ and $\mathbf{m}_{\text{post}}$ are the vectors of "a priori" and "a posteriori" model parameters ($\mathbf{m}_{\text{prior}}$ is the null vector). Vector $\mathbf{d}_{\text{obs}}$ contains the LOS velocity values for all pixels covered by at least one ascending and one descending track after data decimation. We subsample each LOS velocity map using a quadtree algorithm based on the spatial phase gradient [*Welstead*, 1999; *Sudhaus and Jònsson*, 2009]. The maximum quadtree box size is 16 × 16 pixels (approx. 700 × 700 m^2). Because of uncertainties in the fault trace location, we eliminate pixels adjacent to the fault surface trace (less than 0.5 km from the fault; we choose 0.5 km so that slip on the shallowest patches remains constrained). The **G** matrix contains the LOS velocity kernels on each subsampled data point computed for unit slip-rate values on each fault patch. We model the 3D surface displacement using the analytical solution of *Okada* [1985] for a rectangular dislocation embedded in a semi-infinite homogeneous elastic half-space. Projection of these displacements into the LOS takes into account for the incidence angle at each pixel location. Additional terms in **G** are related to the modeling of residual orbital ramps.

[42] The model covariance matrix $\mathbf{C}_{\text{m}}$ is used to smooth the slip-rate solution on the shallow section of the fault [*Radiguet et al.*, 2011]. It is defined as

$$\mathbf{C}_{\text{m}}(\mathbf{i},\mathbf{j}) = \left(\frac{\sigma_{\text{m}}\lambda_0}{\lambda}\right)^2 \mathbf{e}^{\frac{-\mathbf{d}(\mathbf{i},\mathbf{j})}{2\lambda}}, \quad (7)$$

where σ_{m} is the "a priori" standard deviation of the slip-rate model parameters, fixed at 10 mm yr^{-1}, λ is the correlation length (i.e. the characteristic smoothing distance), λ_0 is a scaling factor fixed at 2.5 km, which corresponds to the mean distance between adjacent, shallow patches and $d(i, j)$

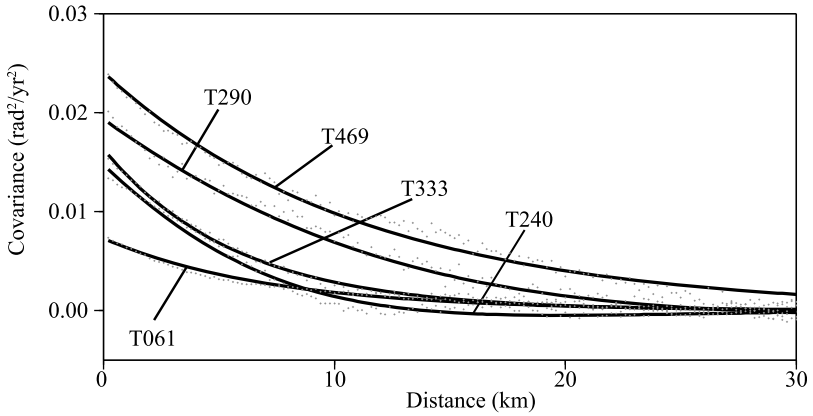

Figure 8. Empirical covariogram (grey dots) and fitted covariance functions (continuous lines) for each track.

is the distance between patches *i* and *j*. The exponential form in equation (7) allows more smoothing at long distances and more variability at small distances than a Gaussian form [*Radiguet et al.*, 2011]. The strike-slip and the dip-slip components on fault patches are independent, so that $\mathbf{C}_m$ is built as two independent blocks, one for each component. "A priori" covariances on the strike-slip rate at depth and on the bilinear ramp terms are assumed independent from any other parameter and set high enough to ensure a sufficient degree of freedom (i.e. practically, we progressively increase σ_m until the best fit parameters are independent from σ_m; Other terms in $\mathbf{C}_m$ are zeros.).

[43] $\mathbf{C}_D$ is the downsampled data covariance matrix that takes into account the residual spatially correlated noise of the mean LOS velocity maps, using the empirical covariance function of each map [*Sudhaus and Jònsson*, 2009], (Figure 8 and Appendix D).

6.2. Inversion Results

[44] We perform the inversion for different values of the correlation lengths λ_{Strike} and λ_{Dip} for the shallow strike-slip and dip-slip rates, respectively. Each solution is characterized by a data-model RMS and a roughness:

$$\rho = \frac{\sum \left| \nabla^2 \mathbf{m}_{\text{post}} \right|}{2N_p}, \tag{8}$$

where $\nabla^2 \mathbf{m}_{\text{post}}$ is the spatial Laplacian of the slip rate distribution and N_p is the number of fault patches [*Jònsson et al.*, 2002]. We use the L-curve criterion to determine the optimal smoothing [*Hansen*, 1992]. Our preferred model is chosen for λ_{Strike} = 12 km and λ_{Dip} = 16 km (Figure 7), as a good compromise between model roughness and the RMS (Figure 9). The "a priori" RMS, computed with $\mathbf{m}_{\mathbf{prior}}$, is ~1 mm yr^{-1}. The "a posteriori" RMS, computed from the preferred $\mathbf{m}_{\text{post}}$, is 0.6 mm yr^{-1}. The fit to data is shown on profiles on Figure 6. Residuals are shown in the auxiliary material as well as three maps showing the modeled East directed, North directed and vertical displacement rate. An oversmoothed model with a large correlation length ($\lambda \gg$ 100 km) would give an "a posteriori" RMS around 0.7 mm yr^{-1}, suggesting that most of the RMS decrease between "a priori" and "a posteriori" models is due to the modeling of

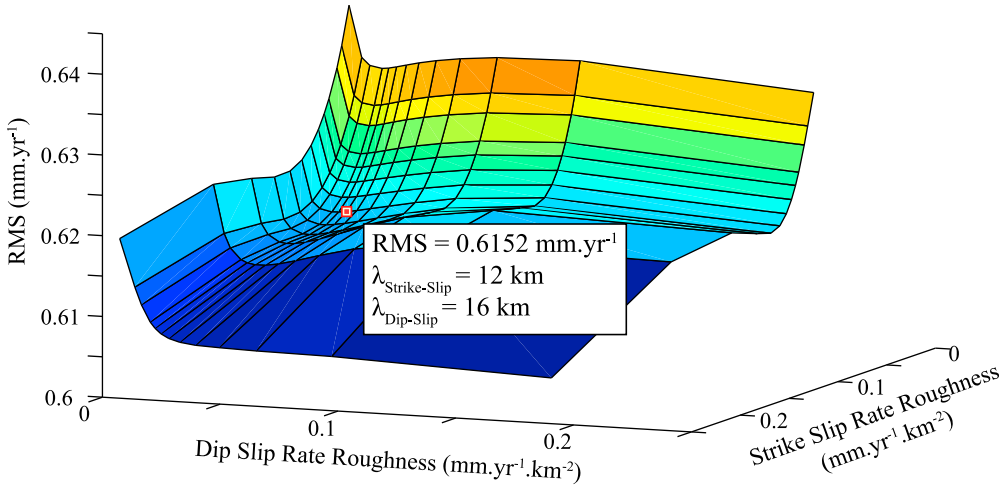

Figure 9. Data-model root mean square as a function of dip-slip rate and strike-slip rate roughnesses. Preferred model is shown by red dot.

the slip rate on the deep section of the fault, fitting far field observations. Uncertainties on the model parameters, as well as trade-offs between parameters (Figure 10), are computed from the "a posteriori" model covariance matrix (details are given in Appendix E).

[45] The inverted, deep left-lateral slip rate is 5.3 ± 1.0 mm yr^{-1}, in overall agreement with previous InSAR or GPS derived studies [*Gan et al.*, 2007; *Cavalié et al.*, 2008]. As the spatial wavelength of the residual orbital ramps is comparable to that of the far field deformation, the deep slip rate is correlated with residual orbital parameters (Figure 10). The correlation is low with the longitude ramp (± 0.2, positive for descending orbits, negative for ascending orbits), and high with the latitude ramp (± 0.7), as expected from the fault orientation. This correlation results in a deep slip rate variation of ~ 0.6 mm yr^{-1}, which remains below the 1σ error on the deep slip rate (~ 1 mm yr^{-1}).

[46] The slip rate on the shallow part of the fault is highly variable (Figure 7). Three distinct sections can be identified.

[47] 1. The western section of the Tianzhu gap, west of the Lao Hu Shan, can be considered as locked. Shallow slip rate values do not exceed 2 mm yr^{-1}, on the order of uncertainties for both slip components.

[48] 2. The fault section that ruptured during the 1920 Haiyuan earthquake appears locked as well. Fault patches at the eastern edge of this section show dip-slip motion. However, they are associated with poor resolution (<0.6) at the model edges. This likely results from the poor data quality in this area, as tracks 290 and 469 have the highest noise level (Figure 8).

[49] 3. In between the two locked sections, a creeping zone is observed along the eastern end of the Tianzhu gap, as inferred from the mean LOS velocity maps (Figure 5). It extends for about 35 km along strike, down to the imposed 20 km depth, with most of the creep concentrated between 5 and 15 km depth. Slip is mostly strike-slip, with a maximum rate of 8 ± 2 mm yr^{-1}, and a mean rate of 5 ± 1.5 mm yr^{-1}. The strong subsidence observed in the Jingtai basin (Figures 5 and 7) is partly explained by a very localized dip-slip motion on the southern bound of the basin, with a rate of 3 ± 0.5 mm yr^{-1} (Figure 6).

[50] The correlation between the estimated strike-slip rates on shallow fault patches and the deep slip rate increases with depth but remains low, below 0.18. The correlation between the shallow dip-slip rate and the deep slip rate is even lower, 0.03 at maximum. This suggests that the inversion of shallow slip rate values is poorly sensitive to the determination of the deep slip rate. Finally, we note that the values of the resolution for the dip-slip values are overall larger than that of the strike-slip values, likely due to the InSAR acquisition geometry.

7. Discussion

7.1. Model Limitations

[51] All previous InSAR studies of interseismic deformation in China rely on the inversion of average LOS velocity profiles across faults, using 2-dimensional fault models in an elastic half-space [*Wright et al.*, 2004; *Taylor and Peltzer*, 2006; *Cavalié et al.*, 2008; *Elliott et al.*, 2008; *Wang et al.*, 2009] or thin plate modeling that takes into account variations in the properties of the medium on both sides of the fault [*Jolivet et al.*, 2008]. Along-strike strain variations are generally neglected. This study shows that such variations can be detected along faults in Tibet, thanks to the large radar data archive acquired by the ERS and Envisat satellites and an appropriate processing scheme, as for the well-documented San Andreas fault in California [e.g., *Ryder and Bürgmann*, 2008].

[52] However, some limitations remain in our modeling related in particular to the simplified geometry and discretization of the modeled fault, and to kinematic assumptions. The deep slip-rate likely varies along-strike, as the fault veers to the South-East and splays into several branches, east of the Yellow river. Indeed, estimates of the long-term Holocene slip rate decrease from west to east [*Lasserre*, 2000; *Li et al.*, 2009]. Furthermore, the deep slip is probably not purely horizontal, given the complex 3-D geometry of the fault system [*Gaudemer et al.*, 1995]. Given the loss of resolution with depth and the difficulty of modeling long spatial wavelengths of the signal, we cannot account for such complexities at depth.

[53] Figure 6 also shows that our model does not correctly reproduce the observed velocity near the fault. The fit could probably be improved by assuming smaller fault patches at shallow depth (i.e. less than 2.5 km depth), a variable correlation length (i.e. smoothing) and introducing slight variations of the fault dip angle along strike at shallow depth.

[54] Finally, we ignore the influence of the Gulang strike-slip fault on the surface velocity field. We quantify below the consequences of this assumption on the estimate of the Haiyuan fault slip-rate.

7.2. Tectonic Loading Rate

[55] The Gulang fault splays eastward from the Haiyuan fault in between the Leng Long Ling and the Jing Qiang He segments and merges with the Tianjing Shan thrust, east of the Yellow river (Figure 1). It acts as a south-dipping lateral thrust ramp branching off the Haiyuan fault [*Gaudemer et al.*, 1995]. Both the Haiyuan fault and the Gulang fault should be taken into account to estimate the present-day tectonic loading between North Eastern Tibet to the South and the Gobi-Ala Shan platform to the North.

[56] A subtle velocity gradient can be seen along the Gulang fault trace in the LOS velocity maps of descending tracks 61, 333 and of the ascending track 240 (Figure 5) and along associated profiles (Figure 6). The velocity gradient is conspicuous near 104°E, about 40 km north of the Haiyuan fault, with several strands forming a wide pushup structure, and becomes sharper near 104.5°E, after stepping to the north (Figures 5, 6a and 6b). However, the Gulang fault related velocity gradient is hardly detectable on the ascending track 469, most likely because of the higher noise level (Figure 8). This velocity change is consistent with left-lateral slip on the Gulang fault, probably combined with North-directed thrust motion, and is about one third of that observed across the Haiyuan fault. This seems consistent with the loading rate difference between the Gulang and Haiyuan faults, estimated from other geodetic (1.3 mm yr^{-1} and 8.6 mm yr^{-1}, respectively [*Gan et al.*, 2007]) or tectonic studies (4 mm yr^{-1} and 10 mm yr^{-1}, respectively [*Gaudemer et al.*, 1995]).

[57] Neglecting the Gulang fault in the modeling partly biases the estimate of the Haiyuan fault deep slip-rate. We therefore test the robustness of our result by masking out

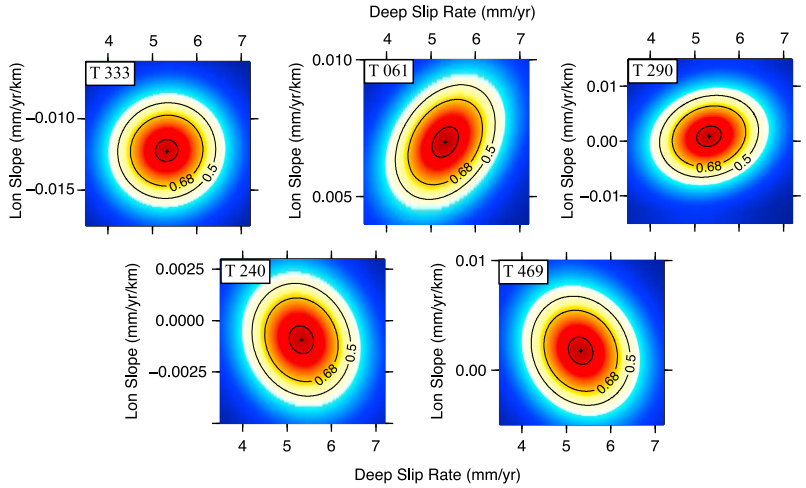

a. Longitude Term

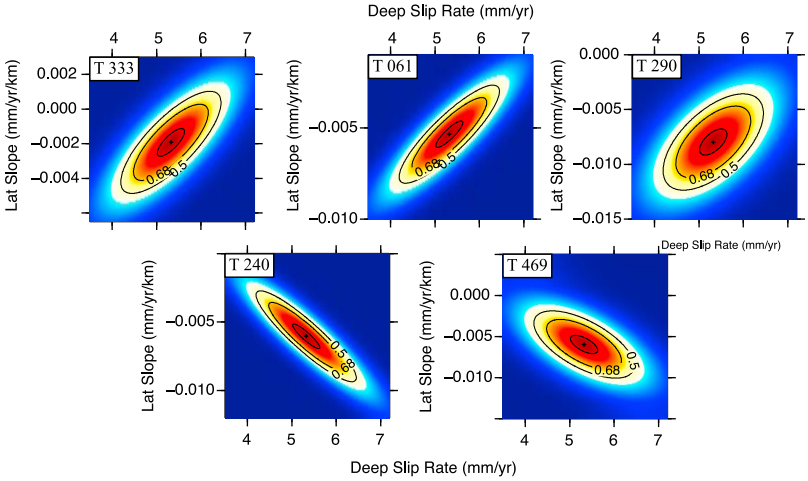

b. Latitude Term

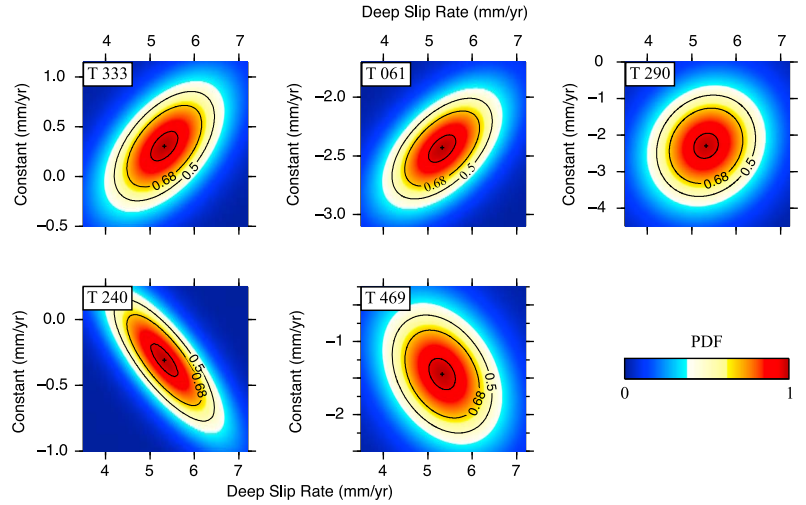

c. Constant

Figure 10. Model parameter tradeoffs: probability density function from the "a posteriori" model covariance matrix between deep slip rate and each of the orbital ramp terms (along longitude, latitude and constant). Contour for PDF values of 0.5, 0.68 (i.e. σ) and 0.95 are shown in black.

the Gulang fault area in the velocity maps and inverting a subset of the surface data around the Haiyuan fault. The "a priori" model RMS for this data subset is 1 mm yr^{-1}, while its "a posteriori" RMS is 0.6 mm yr^{-1}. The inverted parameters slightly differ from those of the previous model: no significant changes are observed on the shallow slip estimates, the residual orbital parameters vary by less than 5% and the deep slip rates are comparable for both models within the error bars (6.1 ± 1 mm yr^{-1} instead of 5.3 ± 1 mm yr^{-1}). We emphasize that further quantification and model refinement are out of the scope of this paper, as an extended study of the 3D geometrical complexity of the fault system at depth would probably require a wider spatial coverage of the area.

[58] Finally, we conclude on a low present-day loading rate of the Haiyuan fault along the studied segments, ~5 mm yr^{-1}. This is in keeping with recent GPS-derived and ERS InSAR studies [*Cavalié et al.*, 2008; *Loveless and Meade*, 2011], but contrasts with the significantly higher estimates of the long-term, Holocene rate on the same fault segment [*Lasserre et al.*, 1999]. Uncertainties on Holocene slip rate estimations as well as complex time varying fault behavior during a single or several seismic cycles could explain such discrepancy [*He and Chery*, 2008].

7.3. Shallow Creep

[59] The existence of a shallow, 35 km-long, slipping zone at the junction between two locked fault segments, one that ruptured during the M_w 8, 1920 earthquake, and one considered as a seismic gap in the late stage of its seismic cycle, is intriguing and raises many questions. The characteristics of this shallow slip, the relationship with the current seismic activity and past earthquakes, the potential mechanisms, as well as the implications on the seismic hazard in the Tianzhu gap area, are discussed below.

[60] The shallow slipping zone along the Lao Hu Shan segment (LHS) is coincident with a cluster of micro-earthquakes, in contrast with the two locked segments on both sides (Figures 1 and 7). Over the observation time period (2003–2009), the geodetic moment released by the shallow slip is $\sim 7.9 \times 10^{17}$ N.m (equation M_w 5.9), more than 30 times larger than the cumulative seismic moment of the recorded earthquakes of $\sim 2.5 \times 10^{16}$ N.m, indicating that most of the observed shallow slip is aseismic. The corresponding average creep rate, ~5 mm yr^{-1}, is similar to the loading rate at depth, suggesting that there is, in overall, no stress increase along the LHS segment between 2003 and 2009. However, locally, the aseismic slip rate reaches values slightly higher than the loading rate (Figure 7). Temporal fluctuations of the creep rate thus may have occurred during the studied period, with episodic bursts that may be related to the microseismic activity.

[61] Similar observations of shallow creep have been made along different sections of the Pacific - North America plate boundary, in California. Reported creep rates along the San Andreas Fault are lower than, or equal to the plate loading rate, and vary along strike [*Lyons and Sandwell*, 2003; *Schmidt et al.*, 2005; *Funning et al.*, 2007; *Ryder and Bürgmann*, 2008] and through time [e.g., *de Michele et al.*, 2011]. Interactions between aseismic slip, microearthquakes and larger earthquakes have been investigated. *Lohman and McGuire* [2007] explain a seismic swarm near the Salton Trough as being driven by aseismic processes, using the rate and state friction formalism [e.g., *Dieterich*, 1994]. *Waldhauser et al.* [2004] suggest that such fault behavior, including creeping and locked segments, and seismicity features at shallow depth, such as streaks of microearthquakes along creeping fault zones [*Rubin et al.*, 1999] or gaps in the seismicity, may relate to long-lived geometrical, frictional or rheological variations along the fault. *Johanson and Burgmann* [2005] suggest that segments devoid of microseismicity are likely locked and prone to generating large ruptures, while segments that exhibit strong micro- to moderate seismic activity mostly release strain by aseismic slip.

[62] We have very few elements to discuss whether the shallow creep process along the Haiyuan fault can be considered as transient or in a steady state at the scale of the seismic cycle. The stress perturbations induced by the 1920 and 1927 earthquakes (both shear stress increase and normal stress decrease along the LHS segment) may have triggered the transient creep and the cluster of microseismicity along this segment. Such a triggering process can be described by rate and state friction laws along velocity strengthening fault segments [*Dieterich*, 1994]. High pressure fluids may circulate in the fault zone and are commonly invoked as contributing to the normal stress decrease on the fault plane, thus favoring transient or steady state creep [*Morrow et al.*, 2000]. Left-lateral slip and reverse slip on a south-dipping Gulang fault should also decrease the normal stress along the Haiyuan fault. However, there is no clear reason why it should occur exclusively on the LHS segment. The fault zone composition and structure may play an important role as well. The presence of weak minerals, like talc, serpentinite or saponite, has been proposed as a mechanism for decreasing the friction coefficient along faults, favoring stable sliding or transient creep at depth as shallow as 0–4 km [*Moore and Rymer*, 2007; *Lockner et al.*, 2011]. In gouge zones in the upper crust, pressure solution mechanism is another possible creep mechanism that may dominate over other processes below a few kilometers from the surface. The nature of grains in the fault gouge, their size and spatial organization strongly influence whether creep is transient or permanent and control the fault seismic behavior [*Gratier et al.*, 2011]. A 500 m-wide shear zone with serpentine boudins has been observed in the LHS, south of the active Haiyuan fault trace. This trace is also marked by a ~60 m-wide gouge zone, containing gypsum crystals [*Lasserre*, 2000].However, shear zones and gouge are observed elsewhere along the fault and not always lead to shallow creep. Further geological and geodetic observations would be necessary to conclude on the mechanisms of the observed creep and its temporal characteristics.

[63] The occurrence of a future large earthquake on the Tianzhu gap remains a plausible threat, with an expected moment magnitude of 8 to break 260 km-long, 20 km-deep fault section bearing a 5 m slip deficit accumulated over 1000 years. Large ruptures often nucleate near major fault bends and jogs [*King and Nabelek*, 1985; *Wesnousky*, 2006], and may result from stable sliding acceleration, as modeled by *Lapusta and Liu* [2009] and recently observed by *Bouchon et al.* [2011]. Because the observed shallow creep on the Haiyuan fault lies at the eastern end of the Tianzhu gap, near a major step over of the fault system, and shows evidence of episodic slip rate increase in the recent years, one may speculate that the LHS fault segment is currently

the locus of a process that will trigger the next large event on the Haiyuan Fault.

8. Conclusion

[64] The time series analysis of interferograms from three descending and two ascending tracks of the Envisat satellite allows us to investigate the spatial variations of interseismic strain along the Haiyuan fault system between 2003 and 2009. The maps of the LOS surface velocity are consistent with a left-lateral motion across the fault and reveal a narrow, ~35 km-long zone of high strain, near the junction between the Tianzhu seismic gap and the fault section, which broke in the 1920, M_w 8 Haiyuan earthquake. The slip rate distribution on the fault plane derived from data inversion shows along-strike variations. At shallow depths (0–20 km), the western part of the Tianzhu gap and the fault section that ruptured in 1920 appear to be locked and are devoid of seismic activity. The 35 km-long Lao Hu Shan segment between the locked sections experiences shallow slip and is coincident with a cluster of micro-earthquakes. This shallow slip is interpreted as due to a creeping process, producing mostly left-lateral movement and a zone of subsidence within the Jingtai pull-apart basin. The average shallow slip-rate (~5 mm yr^{-1}) is comparable in magnitude with the estimated loading rate at depth, assumed to be constant along the fault. This suggests the stress is not increasing on the LHS segment at the present time. However, the data may suggest that some episodic accelerations of the creep have occurred during the study period, a transient process that could be the manifestation of the nucleation mechanism of a future event that may eventually rupture the Tianzhu seismic gap. A better characterization of the inferred transient would require further analysis of the temporal fluctuations of the surface velocity field at the decadal scale, combined with seismological and geological studies. The present study, in agreement with a recent one along the San Andreas fault [*de Michele et al.*, 2011], emphasizes the need for continuous monitoring of creeping segments in the vicinity of major seismic gaps as they should provide hints on seismic hazard assessments.

Appendix A: Image Coregistration

[65] Empirical distortions between master and slave images are first estimated using an amplitude correlation technique. In addition, the slave image distortion in range, with respect to the master image, is predicted using the orbital parameters and the DEM projected in radar geometry at full resolution. The predicted distortion map is then matched to the empirical offset map by adding an optimized translation, before being used as a pixel by pixel grid for resampling the slave image. Distorsions in azimuth are adjusted by a 2D quadratic polynomial:

$$f(R,A) = aA^2 + bRA + cA^2 + dR + eA + f, \qquad \text{(A1)}$$

where R and A are the pixel's range and azimuth, respectively, and a to f are polynomial coefficients to be estimated. This procedure ensures accurate sub-pixel coregistration for large perpendicular baselines and steep topography.

Appendix B: Time Series Analysis

[66] For each pixel of each track, independently, we solve the following system, based on equations (3) and (4):

$$\begin{pmatrix} \Phi_{i,j} \\ \vdots \\ \Phi_{k,l} \\ 0 \\ \vdots \\ 0 \end{pmatrix} = \left(\begin{array}{c|c|ccc} & & 0 & 0 & 0 \\ & D & \vdots & & \vdots \\ & & 0 & 0 & 0 \\ \hline \beta_1 & 0\ 0\ \cdots & 0 & 0 & -B^1_{perp} & -1 \\ \beta_2 & 1\ 0\ \cdots & 0 & -\Delta t_2 & -B^2_{perp} & -1 \\ \beta_3 & 1\ 1\ 0\ \cdots & 0 & -\Delta t_3 & -B^3_{perp} & -1 \\ \gamma\cdot\beta_4 & \vdots & \vdots & \vdots & \vdots & \vdots \\ \vdots & 1\ 1\ 1\ \cdots\ 1\ 0\ 0 & & & & \\ \beta_N & 1\ 1\ 1\ 1\ \cdots\ 1\ 0 & -\Delta t_N & & & -1 \end{array}\right) \begin{pmatrix} \delta\varphi^1 \\ \vdots \\ \delta\varphi^{N-1} \\ V \\ e \\ c \end{pmatrix}. \qquad \text{(B1)}$$

D is the design matrix. β_i are weighting parameters for each image depending on their noise level, as defined in Appendix C. The γ parameter is set low enough (0.01 in our case) so that: (1) the phase increments $\delta\varphi^k$ are fully constrained by equation (3), and equation (4) provides the best fit velocity V and DEM error e; (2) when the inversion is undetermined, equation (4) constrains the phase offset between independent groups of images [*Lopez-Quiroz et al.*, 2009].

Appendix C: Interferogram Selection

[67] We assume that the noise energy function (or spectrum) of an interferogram $\mathrm{Sp}(x)^{i,j}$ (equation (5)) is the sum of the noise energy functions of the two corresponding acquisitions at dates i and j, $\mathrm{Sp}(x)^i$ and $\mathrm{Sp}(x)^j$:

$$\mathrm{Sp}(x)^{i,j} \simeq \mathrm{Sp}(x)^i + \mathrm{Sp}(x)^j. \qquad \text{(C1)}$$

We invert equation (C1) using the least squares solution to estimate each scene noise energy function, their associated errors and resolution [*Tarantola*, 2005]:

$$\mathbf{m} = \left(\mathbf{G}^t\mathbf{C}_D\mathbf{G}\right)^{-1}\mathbf{G}\mathbf{d}, \qquad \text{(C2)}$$

where $\mathbf{d}$ contains the spectrum values of all interferograms, $\mathbf{m}$ contains the spectrum values of all acquisitions and $\mathbf{G}$ is the design matrix. Diagonal terms of the data covariance

matrix $\mathbf{C}_d$ are the variances of the corrected interferograms, while off-diagonal terms are zero.

[68] Each weighting parameter β_i in (equation B1) is the inverse of the spectrum maximum for acquisition i, normalized by the sum of all acquisition spectrum maximum. This way, the relative weight of the constrained part of the matrix (equation (4)) is equal to γ, with respect to the upper part.

Appendix D: Data Covariance Matrix

[69] We compute the empirical semi-variogram of each full-resolution LOS velocity map using the following equation [*Chilès and Delfiner*, 1999]:

$$\gamma(x) = \frac{1}{2N(x)} \sum_{m,n/dist(m,n)=x} (V_m - V_n)^2, \tag{D1}$$

where $\gamma(x)$ is the semi-variogram value at distance x, $N(x)$ is the number of pixel pairs separated by the distance x and V_m and V_n are the LOS velocities of pixels m and n. As for the energy function in equation (5), there exists a sill value γ_S over a distance of ≃30 km beyond which noise is uncorrelated. Considering the residual noise as second-order stationary (i.e. not dependent on the position) and isotropic, it is possible to build the two dimensional covariance function $Cov(x)$ for each LOS velocity map from the semi-variogram using the following equation:

$$Cov(x) = \gamma_S - \gamma(x). \tag{D2}$$

Following *Sudhaus and Jònsson* [2009], we fit each covariance function either with an exponential decay $a.\ e^{-bx}$ or an exponential decay combined with a cosine term $a.\ e^{-bx}\cos(wx)$ (Table 1 and Figure 8). To ensure that the covariance functions remain positive-definite, we impose $w < b$ [*Chilès and Delfiner*, 1999]. We use these covariance functions to build the full data covariance matrix $\mathbf{C}_{Df}$. The downsampled data covariance matrix $\mathbf{C}_D$ used in equation (6) is related to $\mathbf{C}_{Df}$ through the linear quadtree operator $\mathbf{Q}$ [*Sudhaus and Jònsson*, 2009]:

$$\mathbf{C}_D = \mathbf{Q}\mathbf{C}_{Df}. \tag{D3}$$

This ensures a high (respectively low) weight to data points representing a large (respectively small) area.

Appendix E: Inversion Quality Tools From *Tarantola* [2005]

[70] A posteriori errors on the model parameters are given by

$$\mathbf{C}_{mpost} = \left(\mathbf{G}^t\mathbf{C}_D^{-1}\mathbf{G} + \mathbf{C}_m^{-1}\right)^{-1}, \tag{E1}$$

where $\mathbf{G}$ is the theory matrix, $\mathbf{C}_D$ is the data covariance matrix (D) and $\mathbf{C}_m$ is the model covariance matrix. The diagonal terms of $\mathbf{C}_{mpost}$ are the variance of each parameter, while the non-diagonal terms give the covariances between parameters.

[71] The correlation ρ_{ij} between two parameters i and j (−1, 0 and 1 for anti-correlated, not correlated and correlated, respectively) is defined as

$$\rho_{ij} = \frac{\mathbf{C}_{mpost}(i,j)}{\sqrt{\mathbf{C}_{mpost}(i,i)\mathbf{C}_{mpost}(\mathbf{j},\mathbf{j})}}. \tag{E2}$$

[72] The resolution operator $\mathbf{R}$ is given by

$$\mathbf{R} = \mathbf{C}_m\mathbf{G}^t\left(\mathbf{G}\mathbf{C}_m\mathbf{G}^t + \mathbf{C}_D\right)^{-1}\mathbf{G}. \tag{E3}$$

Because we impose a spatial smoothing on fault patches through the model covariance matrix $\mathbf{C}_m$, slip value on a patch depends on the slip of the neighboring patches. We thus express the resolution of each slip parameter as the sum of all terms in the corresponding line of the resolution operator $\mathbf{R}$. A fully resolved (respectively unresolved) parameter has a resolution of 1 (respectively 0).

[73] **Acknowledgments.** The SAR data set was provided by the European Space Agency (ESA) in the framework of the Dragon 2 program (ID 2509 and 5305). This program also supported R. Jolivet's work, through the Young Scientist fellowship. Funding was provided by the French "Extraction et Fusion d'Information et de Données d'Interférométrie Radar" program (EFIDIR, ANR, France) and Programme National de Télédétection Spatiale (CNES). Part of G. Peltzer's contribution was done at the Jet Propulsion Laboratory, California Institute of Technology, under contract with NASA. Figures and map were prepared using Generic Mapping Tools software [*Wessel and Smith*, 1995]. The authors thank Gareth Funning, an anonymous reviewer, and the Associate Editor for their constructive comments and suggestions.

References

Ambraseys, N. N. (1970), Some characteristic features of anatolian fault zone, *Tectonophysics*, *9*(2–3), 143–165.

Anderson, E., et al. (1999), *LAPACK Users' Guide*, 3rd ed., Soc. for Indust. and Appl. Math., Philadelphia, Penn.

Berardino, P., G. Fornaro, R. Lanari, and E. Santosti (2002), A new algorithm for surface deformation monitoring based on small baseline differential SAR interferograms, *IEEE Trans. Geosci. Remote Sens.*, *40*(11), 2375–2383, doi:10.1109/TGRS.2002.803792.

Biggs, J., T. Wright, Z. Lu, and B. Parsons (2007), Multi-interferogram method for measuring interseismic deformation: Denali fault, Alaska, *Geophys. J. Int.*, *170*(3), 1165–1179, doi:10.1111/j.1365-246X.2007.03415.x.

Bouchon, M., H. Karabulut, M. Aktar, S. Ozalaybey, J. Schmittbuhl, and M.-P. Bouin (2011), Extended nucleation of the 1999 M-w 7.6 Izmit earthquake, *Science*, *331*(6019), 877–880, doi:10.1126/science.1197341.

Cavalié, O., M. P. Doin, C. Lasserre, and P. Briole (2007), Ground motion measurement in the Lake Mead area, Nevada, by differential synthetic aperture radar interferometry time series analysis: Probing the lithosphere rheological structure, *J. Geophys. Res.*, *112*, B03403, doi:10.1029/2006JB004344.

Cavalié, O., C. Lasserre, M. P. Doin, G. Peltzer, J. Sun, X. Xu, and Z. K. Shen (2008), Measurement of interseismic strain across the Haiyuan fault (Gansu, China), by InSAR, *Earth Planet. Sci. Lett.*, *275*(3–4), 246–257, doi:10.1016/j.epsl.2008.07.057.

Çakir, Z., A. Akoglu, S. Belabbes, S. Ergintav, and M. Meghraoui (2005), Creeping along the ismetpasa section of the North Anatolian fault (western Turkey): Rate and extent from InSAR, *Earth Planet. Sci. Lett.*, *238*(1–2), 225–234, doi:10.1016/j.epsl.2005.06.044.

Chilès, J.-P., and P. Delfiner (1999), *Geostatistics - Modeling Spatial Uncertainty*, John Wiley, New York.

Chlieh, M., J. P. Avouac, K. Sieh, D. H. Natawidjaja, and J. Galetzka (2008), Heterogeneous coupling of the Sumatran megathrust constrained by geodetic and paleogeodetic measurements, *J. Geophys. Res.*, *113*, B05305, doi:10.1029/2007JB004981.

Cowgill, E. (2007), Impact of riser reconstructions on estimation of secular variation in rates of strike-slip faulting: Revisiting the Cherchen River site along the Altyn Tagh Fault, NW China, *Earth Planet. Sci. Lett.*, *254*(3–4), 239–255, doi:10.1016/j.epsl.2006.09.015.

de Michele, M., D. Raucoules, F. Rolandone, P. Briole, J. Salichon, A. Lemoine, and H. Aochi (2011), Spatiotemporal evolution of surface

creep in the Parkfield region of the San Andreas fault (1993–2004) from synthetic aperture radar, *Earth Planet. Sci. Lett.*, *308*(1–2), 141–150, doi:10.1016/j.epsl.2011.05.049.

Deng, Q., et al. (1986), Variations in the geometry and amount of slip on the Haiyuan (Nanxihaushan) fault zone, China, and the surface rupture of the 1920 Haiyuan earthquake, in *Earthquake Source Mechanism*, *Geophys. Monogr. Ser.*, vol. 37, pp. 169–182, edited by S. Das, J. Boatwright, and C. Scholtz, AGU, Washington, D. C.

Dieterich, J. H. (1994), A constitutive law for rate of earthquake production an its application to earthquake clustering, *J. Geophys. Res.*, *99*, 2601–2618, doi:10.1029/93JB02581.

Doin, M. P., C. Lasserre, G. Peltzer, O. Cavalie, and C. Doubre (2009), Corrections of stratified tropospheric delays in SAR interferometry: Validation with global atmospheric models, *J. Appl. Geophys.*, *69*, 35–50, doi:10.1016/j.jappgeo.2009.03.010.

Doin, M. P., S. Guillaso, R. Jolivet, C. Lasserre, F. Lodge, G. Ducret, and R. Grandin (2011), Presentation of the small baseline NSBAS processing chain on a case example: The etna deformation monitoring from 2003 to 2010 using ENVISAT data, *Eur. Space Agency Spec. Publ.*, *ESA SP-697*, 1–7.

Doubre, C., and G. Peltzer (2007), Fluid-controlled faulting process in the Asal Rift, Djibouti, from 8 yr of radar interferometry observations, *Geology*, *35*(1), 69–72, doi:10.1130/G23022A.1.

Dragert, H., K. Wang, and T. S. James (2001), A silent slip event on the deeper Cascadia subduction interface, *Science*, *292*(5521), 1525–1528, doi:10.1126/science.1060152.

Elliott, J. R., J. Biggs, B. Parsons, and T. J. Wright (2008), InSAR slip rate determination on the Altyn Tagh Fault, northern Tibet, in the presence of topographically correlated atmospheric delays, *Geophys. Res. Lett.*, *35*, L12309, doi:10.1029/2008GL033659.

Farr, T. G., and M. Kobrick (2000), Shuttle radar topography mission produces a wealth of data, *Eos Trans. AGU*, *81*(48), 583–585.

Ferretti, A., C. Prati, and F. Rocca (2001), Permanent scatterers in SAR interferometry, *IEEE Trans. Geosci. Remote Sens.*, *39*(1), 8–20.

Funning, G. J., R. Bürgmann, A. Ferretti, F. Novali, and A. Fumagalli (2007), Creep on the Rodgers Creek Fault, northern San Francisco bay area from 10 year ps-insar data set, *Geophys. Res. Lett.*, *34*, L19306, doi:10.1029/2007GL030836.

Gan, W., P. Z. Zhang, Z.-K. Shen, Z. Niu, M. Wang, Y. Wan, D. Zhou, and J. Cheng (2007), Present-day crustal motion within the Tibetan Plateau inferred from GPS measurements, *J. Geophys. Res.*, *112*, B08416, doi:10.1029/2005JB004120.

Gaudemer, Y., P. Tapponnier, B. Meyer, G. Peltzer, S. M. Guo, Z. T. Chen, H. G. Dai, and I. Cifuentes (1995), Partitioning of crustal slip between linked, active faults in the eastern Qilian Shan, and evidence for a major seismic gap, the Tianzhu Gap, on the western Haiyuan Fault, Gansu (China), *Geophys. J. Int.*, *120*(3), 599–645.

Goldstein, M. R., and L. C. Werner (1998), Radar interferogram filtering for geophysical applications, *Geophys. Res. Lett.*, *25*(21), 4035–4038, doi:10.1029/1998GL900033.

Goldstein, M. R., A. H. Zebker, and C. L. Werner (1988), Satellite radar interferometry: Two-dimensional phase unwrapping, *Radio Sci.*, *23*(4), 713–720, doi:10.1029/RS023i004p00713.

Gourmelen, N., F. Amelung, and R. Lanari (2010), Interferometric synthetic aperture radar-GPS integration: Interseismic strain accumulation across the hunter mountain fault in the eastern California shear zone, *J. Geophys. Res.*, *115*, B09408, doi:10.1029/2009JB007064.

Gratier, J.-P., J. Richard, J. Renard, F. Mittempergher, M.-L. Doan, G. Di Toro, J. Hadizadeh, and A.-M. Boullier (2011), Aseismic sliding of active faults by pressure solution creep: Evidence from the san andreas fault observatory at depth, *Geology*, *39*, 1131–1134.

Guillaso, S., A. Reigber, L. Ferro-Famil, and E. Pottier (2006), Range resolution improvement of airborne SAR images, *IEEE Geosci. Remote Sens. Lett.*, *3*(1), 135–139, doi:10.1109/LGRS.2005.859943.

Guillaso, S., C. Lasserre, M.-P. Doin, O. Cavalié, J. Sun, and G. Peltzer (2008), InSAR measurement of interseismic strain in areas of low coherence: Example across the Haiyuan Fault (Gansu, China) using a local InSAR adaptive range filter, paper presented at General Assembly, Eur. Geosci. Union, Vienna.

Hansen, P. C. (1992), Analysis of discrete ill-posed problems by means of the L-curve, *SIAM Rev.*, *34*(4), 561–580.

He, J., and J. Chery (2008), Slip rates of the Altyn Tagh, Kunlun and Karakorum faults (Tibet) from 3D mechanical modeling, *Earth Planet. Sci. Lett.*, *274*(1–2), 50–58, doi:10.1016/j.epsl.2008.06.049.

Hetland, E., and B. Hager (2006), Interseismic strain accumulation: Spin-up, cycle invariance, and irregular rupture sequences, *Geochem. Geophys. Geosyst.*, *7*, Q05004, doi:10.1029/2005GC001087.

Hooper, A., P. Segall, and H. Zebker (2007), Persistent scatterer interferometric synthetic aperture radar for crustal deformation analysis, with application to Volcan Alcedo, Galapagos, *J. Geophys. Res.*, *112*, B07407, doi:10.1029/2006JB004763.

Johanson, I., and R. Burgmann (2005), Creep and quakes on the northern transition zone of the San Andreas fault from GPS and InSAR data, *Geophys. Res. Lett.*, *32*, L14306, doi:10.1029/2005GL023150.

Jolivet, R., R. Cattin, N. Chamot-Rooke, C. Lasserre, and G. Peltzer (2008), Thin-plate modelling of interseismic deformation and asymmetry across the Altyn Tagh fault zone, *Geophys. Res. Lett.*, *35*, L02309, doi:10.1029/2007GL031511.

Jolivet, R., R. Bürgmann, and N. Houlié (2009), Geodetic exploration of the elastic properties across and within the northern San Andreas fault zone, *Earth Planet. Sci. Lett.*, *288*(1-2), 126–131, doi:10.1016/j.epsl.2009.09.014.

Jolivet, R., R. Grandin, C. Lasserre, M.-P. Doin, and G. Peltzer (2011), Systematic InSAR tropospheric phase delay corrections from globa meteorological reanalysis data, *Geophys. Res. Lett.*, *38*, L17311, doi:10.1029/2011GL048757.

Jònsson, S., H. A. Zebker, P. Segall, and F. Amelung (2002), Fault slip distribution of the 1999 M_w7.1 Hector Mine, California, earthquake, estimated from satellite radar and GPS measurements, *Bull. Seismol. Soc. Am.*, *92*(4), 1377–1389, doi:10.1785/0120000922.

King, G., and J. Nabelek (1985), Role of fault bends in the initiation and termination of earthquake rupture, *Science*, *228*(4702), 984–987, doi:10.1126/science.228.4702.984.

Kostoglodov, V., S. Singh, J. Santiago, S. Franco, K. Larson, A. Lowry, and R. Bilham (2003), A large silent earthquake in the Guerrero seismic gap, Mexico, *Geophys. Res. Lett.*, *30*(15), 1807, doi:10.1029/2003GL017219.

Lapusta, N., and Y. Liu (2009), Three-dimensional boundary integral modeling of spontaneous earthquake sequences and aseismic slip, *J. Geophys. Res.*, *114*, B09303, doi:10.1029/2008JB005934.

Lasserre, C. (2000), Fonctionnement sismique, cinématique et histoire géologique de la faille de haiyuan, PhD thesis, Univ. Paris 7, Paris.

Lasserre, C. P., et al. (1999), Postglacial left slip rate and past occurrence of M 8 earthquakes on the western Haiyuan fault, Gansu, China, *J. Geophys. Res.*, *104*(B8), 17,633–17,651, doi:10.1029/1998JB900082.

Lasserre, C., B. Bukchin, P. Bernard, P. Tapponnier, Y. Gaudemer, A. Mostinsky, and R. Dailu (2001), Source parameters and tectonic origin of the 1996 June 1 Tianzhu (M-w = 5.2) and 1995 July 21 Yongden (M-w = 5.6) earthquakes near the Haiyuan fault (Gansu, China), *Geophys. J. Int.*, *144*(1), 206–220, doi:10.1046/j.1365-246x.2001.00313.x.

Lasserre, C., Y. Gaudemer, P. Tapponnier, A. S. Mériaux, J. Van der Woerd, Y. Daoyang, F. J. Ryerson, R. C. Finkel, and M. W. Caffee (2002), Fast late pleistocene slip rate on the Leng Long Ling segment of the Haiyuan fault, Qinghai, China, *J. Geophys. Res.*, *107*(B11), 2276, doi:10.1029/2000JB000060.

Li, C., P. Z. Zhang, J. Yin, and W. Min (2009), Late quaternary left-lateral slip rate of the Haiyuan fault, northeastern margin of the Tibetan Plateau, *Tectonics*, *28*, TC5010, doi:10.1029/2008TC002302.

Lienkaemper, J. J., G. Borchardt, and M. Lisowski (1991), Historic creep rate and potential for seismic slip along the Hayward fault, California, *J. Geophys. Res.*, *96*(B11), 18,261–18,283, doi:10.1029/91JB01589.

Liu-Zeng, J., Y. Klinger, X. Xu, C. Lasserre, G. Chen, W. Chen, P. Tapponnier, and B. Zhang (2007), Millennial recurrence of large earthquakes on the Haiyuan fault near Songshan, Gansu Province, China, *Bull. Seismol. Soc. Am.*, *97*, 14–34, doi:10.1785/0120050118.

Lockner, D. A., C. Morrow, D. Moore, and S. Hickman (2011), Low strength of deep San Andreas fault gouge from SAFOD core, *Nature*, *472*, 82–85, doi:10.1038/nature09927.

Lohman, R. B., and J. J. McGuire (2007), Earthquake swarms driven by aseismic creep in the Salton Trough, California, *J. Geophys. Res.*, *112*, B04405, doi:10.1029/2006JB004596.

Lopez-Quiroz, P., M.-P. Doin, F. Tupin, P. Briole, and J.-M. Nicolas (2009), Time series analysis of Mexico City subsidence constrained by radar interferometry, *J. Appl. Geophys.*, *69*, 1–15, doi:10.1016/j.jappgeo.2009.02.006.

Loveless, J., and B. Meade (2011), Partitioning of localized and diffuse deformation in the Tibetan Plateau from joint inversions of geologic and geodetic observations, *Earth Planet. Sci. Lett.*, *303*(1-2), 11–24, doi:10.1016/j.epsl.2010.12.014.

Lundgren, P., E. A. Hetland, Z. Liu, and E. J. Fielding (2009), Southern San Andreas-San Jacinto fault system slip rates estimated from earthquake cycle models constrained by GPS and interferometric synthetic aperture radar observations, *J. Geophys. Res.*, *114*, B02403, doi:10.1029/2008JB005996.

Lyons, S., and D. Sandwell (2003), Fault creep along the southern San Andreas from interferometric synthetic aperture radar, permanent scatterers, and stacking, *J. Geophys. Res.*, *108*(B1), 2047, doi:10.1029/2002JB001831.

Mazzotti, S., X. Le Pichon, P. Henry, and S. Miyazaki (2000), Full interseismic locking of the Nankai and Japan-west Kurile subduction zones: An analysis of uniform elastic strain accumulation in Japan constrained by permanent GPS, *J. Geophys. Res.*, *105*(B6), 13,159–13,177, doi:10.1029/2000JB900060.

Mériaux, A. S., F. J. Ryerson, P. Tapponnier, J. Van der Woerd, R. C. Finkel, X. Xu, Z. Xu, and M. W. Caffe (2004), Rapid slip along the central Altyn Tagh Fault: Morphochronologic evidence from Cherchen He and Sulamu Tagh, *J. Geophys. Res.*, *109*, B06401, doi:10.1029/2003JB002558.

Meyer, B., P. Tapponnier, L. Bourjot, F. Metivier, Y. Gaudemer, G. Peltzer, G. Shunmin, and C. Zhitai (1998), Crustal thickening in Gansu-Qinghai, lithospheric mantle subduction, and oblique, strike-slip controlled growth of the Tibet Plateau, *Geophys. J. Int.*, *135*(1), 1–47.

Moore, D. E., and M. J. Rymer (2007), Talc-bearing serpentinite and the creeping section of the San Andreas fault, *Nature*, *448*, 795–797, doi:10.1038/nature06064.

Morrow, C. A., D. E. Moore, and D. A. Lockner (2000), The effect of mineral bond strength and adsorbed water on fault gouge frictional strength, *Geophys. Res. Lett.*, *27*, 815–818, doi:10.1029/1999GL008401.

Nitti, D. O., R. F. Hanssen, A. Refice, F. Bovenga, and R. Nutricato (2011), Impact of DEM-assisted coregistration on high-resolution SAR interferometry, *Geosci. Remote Sens. Lett.*, *49*(3), 1127–1143, doi:10.1109/TGRS.2010.2074204.

Okada, Y. (1985), Surface deformation due to shear and tensile faults in a half-space, *Bull. Seismol. Soc. Am.*, *75*(4), 1135–1154.

Ozawa, S., M. Murakami, M. Kaidzu, T. Tada, T. Sagiya, Y. Hatanaka, H. Yarai, and T. Nishimura (2002), Detection and monitoring of ongoing aseismic slip in the Tokai region, central Japan, *Science*, *298*(5595), 1009–1012, doi:10.1126/science.1076780.

Peltzer, G., F. Crampe, S. Hensley, and P. Rosen (2001), Transient strain accumulation and fault interaction in the eastern California shear zone, *Geology*, *29*(11), 975–978, doi:10.1130/0091-7613(2001)029.

Puysségur, B., R. Michel, and J.-P. Avouac (2007), Tropospheric phase delay in interferometric synthetic aperture radar estimated from meteorological model and multispectral imagery, *J. Geophys. Res.*, *112*, B05419, doi:10.1029/2006JB004352.

Radiguet, M., F. Cotton, M. Vergnolle, M. Campillo, B. Valette, V. Kostoglodov, and N. Cotte (2011), Spatial and temporal evolution of a long term slow slip event: The 2006 Guerrero slow slip event, *Geophys. J. Int.*, *184*(2), 816–828, doi:10.1111/j.1365-246X.2010.04866.x.

Rosen, P., S. Hensley, G. Peltzer, and M. Simons (2004), Updated repeat orbit interferometry package released, *Eos Trans. AGU*, *85*(5), 47.

Rubin, A., D. Gillard, and J. Got (1999), Streaks of microearthquakes along creeping faults, *Nature*, *400*(6745), 635–641, doi:10.1038/23196.

Ryder, I., and R. Bürgmann (2008), Spatial variations in slip deficit on the central San Andreas fault from InSAR, *Geophys. J. Int.*, *175*(3), 837–852, doi:10.1111/j.1365-246X.2008.03938.x.

Savage, J. C., and R. O. Burford (1973), Geodetic determination of relative plate motion in central California, *J. Geophys. Res.*, *78*, 832–845, doi:10.1029/JB078i005p00832.

Schmidt, D. A., and R. Bürgmann (2003), Time-dependent land uplift and subsidence in the Santa Clara valley, California, from a large interferometric synthetic aperture radar data set, *J. Geophys. Res.*, *108*(B9), 2416, doi:10.1029/2002JB002267.

Schmidt, D. A., R. Burgmann, R. M. Nadeau, and M. d'Alessio (2005), Distribution of aseismic slip rate on the Hayward fault inferred from seismic and geodetic data, *J. Geophys. Res.*, *110*, B08406, doi:10.1029/2004JB003397.

Sudhaus, H., and S. Jònsson (2009), Improved source modelling through combined use of InSAR and GPS under consideration of correlated data errors: Application to the June 2000 Kleifarvatn earthquake, Iceland, *Geophys. J. Int.*, *176*(2), 389–404, doi:10.1111/j.1365-246X.2008.03989.x.

Tarantola, A. (2005), *Inverse Problem Theory and Methods for Model Parameter Estimation*, Soc. for Indust. and Appl. Math., Philadelphia, Penn.

Taylor, M., and G. Peltzer (2006), Current slip rates on conjugate strike-slip faults in central Tibet using synthetic aperture radar interferometry, *J. Geophys. Res.*, *111*, B12402, doi:10.1029/2005JB004014.

Uppala, S. M., et al. (2005), The ERA-40 re-analysis, *Q. J. R. Meteorol. Soc.*, *131*, 2961–3012, doi:10.1256/qj.04.176.

Usai, S. (1999), SAR interferometry on a very long time scale: A study of the interferometric characteristics of man-made features, *IEEE Trans. Geosci. Remote Sens.*, *37*(4), 2118–2123.

Waldhauser, F., W. L. Ellsworth, D. P. Schaff, and A. Cole (2004), Streaks, multiplets, and holes: High-resolution spatio-temporal behavior of Parkfield seismicity, *Geophys. Res. Lett.*, *31*, L18608, doi:10.1029/2004GL020649.

Wang, H., T. J. Wright, and J. Biggs (2009), Interseismic slip rate of the northwestern Xianshuihe fault from InSAR data, *Geophys. Res. Lett.*, *36*, L03302, doi:10.1029/2008GL036560.

Welstead, S. T. (1999), *Fractal and Wavelet Image Compression Technique*, Int. Soc. for Opt. and Photon. Opt. Eng. Press, Bellingham, Wash.

Wesnousky, S. G. (2006), Predicting the endpoints of earthquake ruptures, *Nature*, *444*(7117), 358–360, doi:10.1038/nature05275.

Wessel, P., and W. Smith (1995), New version of the Generic Mapping Tools released, *Eos Trans. AGU*, *76*(33), 329.

Wright, T., B. Parsons, and E. Fielding (2001), Measurement of interseismic strain accumulation across the North Anatolian Fault by satellite radar interferometry, *Geophys. Res. Lett.*, *28*(10), 2117–2120, doi:10.1029/2000GL012850.

Wright, T. J., B. Parsons, P. C. England, and E. Fielding (2004), InSAR observations of low slip rates on the major faults of western Tibet, *Science*, *305*, 236–239, doi:10.1126/science.1096388.

Xu, X., R. S. Yeats, and G. Yu (2010), Five short historical earthquake surface ruptures near the Silk Road, Gansu Province, China, *Bull. Seismol. Soc. Am.*, *100*(2), 541–561, doi:10.1785/0120080282.

Zebker, H. A., and J. Villasenor (1992), Decorrelation in interferometric radar echoes, *IEEE Trans. Geosci. Remote Sens.*, *30*(5), 950–959.

Zebker, H. A., P. A. Rosen, and S. Hensley (1997), Atmospheric effects in interferometric synthetic aperture radar surface deformation and topographic maps, *J. Geophys. Res.*, *102*(B4), 7547–7563, doi:10.1029/96JB03804.

Zhang, W. Q., D. C. Jiao, P. Z. Zhang, P. Molnar, B. C. Burchfield, Q. D. Deng, Y. P. Wang, and F. M. Song (1987), Displacement along the Haiyuan fault associated with the great 1920 Haiyuan, China, earthquake, *Bull. Seismol. Soc. Am.*, *77*(1), 117–131.

Zhang, P. Z., P. Molnar, B. C. Burchfield, L. Royden, Y. P. Wang, Q. D. Deng, F. M. Song, W. Q. Zhang, and D. C. Jiao (1988), Bounds on the Holocene slip rate of the Haiyuan Fault, north-central China, *Quat. Res.*, *30*(2), 151–164.